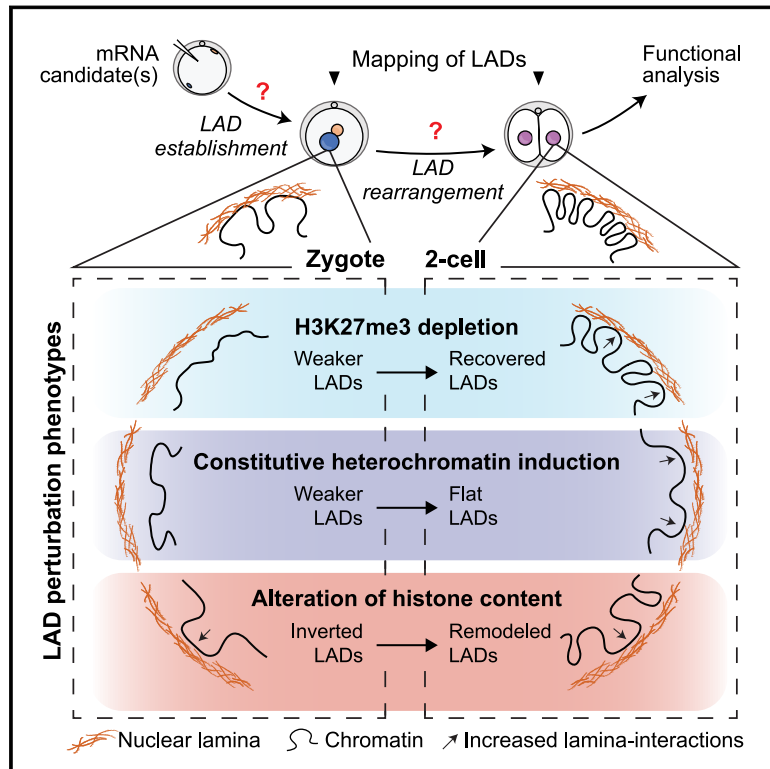# The establishment of nuclear organization in mouse embryos is orchestrated by multiple epigenetic pathways

Graphical abstract

Authors

Mrinmoy Pal, Tamas Schauer, Adam Burton, ..., Iliya Nadelson, Marc A. Marti-Renom, Maria-Elena Torres-Padilla

Correspondence

torres-padilla@helmholtz-muenchen.de

In brief

In vivo screening in mouse embryos provides insights into the functional interplay between chromatin and the nuclear envelope in the establishment of lamina-associated domains, the earliest feature of nuclear organization following fertilization.

Highlights

- Low-input genomics screening *in vivo* generates a resourceful dataset in mouse embryos

- Embryos can rebuild LAD architecture at the 2-cell stage when disrupted in zygotes

- Maternal H3K27me3 inheritance over *de novo* methylation shapes zygotic LAD formation

- LAD boundaries reorganize from positional information of H3K4me3 and H3K9me3 domains

CellPress

Cell

Resource

The establishment of nuclear organization in mouse embryos is orchestrated by multiple epigenetic pathways

Mrinmoy Pal,[1] Tamas Schauer,[1] Adam Burton,[1] Tsunetoshi Nakatani,[1] Federico Pecori,[1] Alicia Hernández-Giménez,[2] Iliya Nadelson,[1] Marc A. Marti-Renom,[2,3,4,5] and Maria-Elena Torres-Padilla[1,6,7,*]

[1]Institute of Epigenetics and Stem Cells, Helmholtz Munich, Munich, Germany
[2]National Center for Genome Analysis, Baldiri Reixac 4, 08028 Barcelona, Spain
[3]Centre for Genomic Regulation, Barcelona Institute for Science and Technology, Carrer del Doctor Aiguader 88, 08003 Barcelona, Spain
[4]ICREA, Pg. Lluís Companys 23, 08010 Barcelona, Spain
[5]Universitat Pompeu Fabra, 08002 Barcelona, Spain
[6]Faculty of Biology, Ludwig-Maximilians University, Munich, Germany
[7]Lead contact
*Correspondence: torres-padilla@helmholtz-muenchen.de
https://doi.org/10.1016/j.cell.2025.03.044

SUMMARY

The folding of the genome in the 3D nuclear space is fundamental for regulating all DNA-related processes. The association of the genome with the nuclear lamina into lamina-associated domains (LADs) represents the earliest feature of nuclear organization during development. Here, we performed a gain-of-function screen in mouse embryos to obtain mechanistic insights. We find that perturbations impacting histone H3 modifications, heterochromatin, and histone content are crucial for the establishment of nuclear architecture in zygotes and/or 2-cell-stage embryos. Notably, some perturbations exerted differential effects on zygotes versus 2-cell-stage embryos. Moreover, embryos with disrupted LADs can rebuild nuclear architecture at the 2-cell stage, indicating that the initial establishment of LADs in zygotes might be dispensable for early development. Our findings provide valuable insights into the functional interplay between chromatin and structural components of the nucleus that guide genome-lamina interactions during the earliest developmental stages.

INTRODUCTION

The higher-order genome structure regulates all DNA-dependent processes, rendering specific sequences accessible for transcription[1] and protecting DNA from damage.[2] Chromosomes undergo long-range intrachromosomal interactions, forming A and B compartments[3] and topologically associating domains (TADs).[4–6] A-compartment largely encompasses active chromatin regions of higher chromatin accessibility replicating early during S-phase. B compartments comprise heterochromatic regions, replicate later, and are largely inaccessible.[4,7,8] The genome also organizes around nuclear landmarks. Among these, organization into lamina-associated domains (LADs) is a major pillar of three-dimensional (3D)-genome organization. LADs are large genomic regions of 100 kb to 10 Mb that associate with the nuclear lamina.[9–12]

LADs share distinctive features, including high AT content, low gene density, and overall repressed chromatin.[11,13] Generally, LADs replicate late during S-phase and correspond to B compartments, while inter-LADs (iLADs) replicate early and correspond to A compartments.[8,10,14] iLADs display higher transcrip-

tional activity, and transcriptional units can detach from the nuclear lamina upon activation.[15–17] In some cell types, LAD boundaries are delineated by sharp changes in H3K4me2 and H3K27me3.[10,18] In differentiated and embryonic stem cells (ESCs), LADs are enriched in H3K9me2,[10,19,20] and inhibiting the H3K9 methyltransferase EHMT2 reduces LAD-nuclear-lamina contacts.[18,21,22] However, disrupting nuclear-lamina components, including lamins, results in a largely unaffected LAD landscape,[23] suggesting that LADs are robust once established.

Previous work using LaminB1-DNA adenine methyltransferase identification (DamID) in oocytes and early mouse embryos revealed that LADs are undetectable in interphase nuclei of mature oocytes but rapidly establish after fertilization.[24] LADs are subsequently remodeled prior to the completion of maternal-to-zygotic transition (MZT) at the 2-cell stage. This reorganization occurs after the first mitosis and throughout the second cell cycle.[24,25] Despite unusual LAD features at the 2-cell stage, this reorganization correlates with transcription as the 2-cell-stage-specific LADs overall contain silent genes.[24,25] Remarkably, ~40% of the genome in mouse zygotes constitutes constant LADs, genomic regions that are LADs across cell types,

Cell
Resource
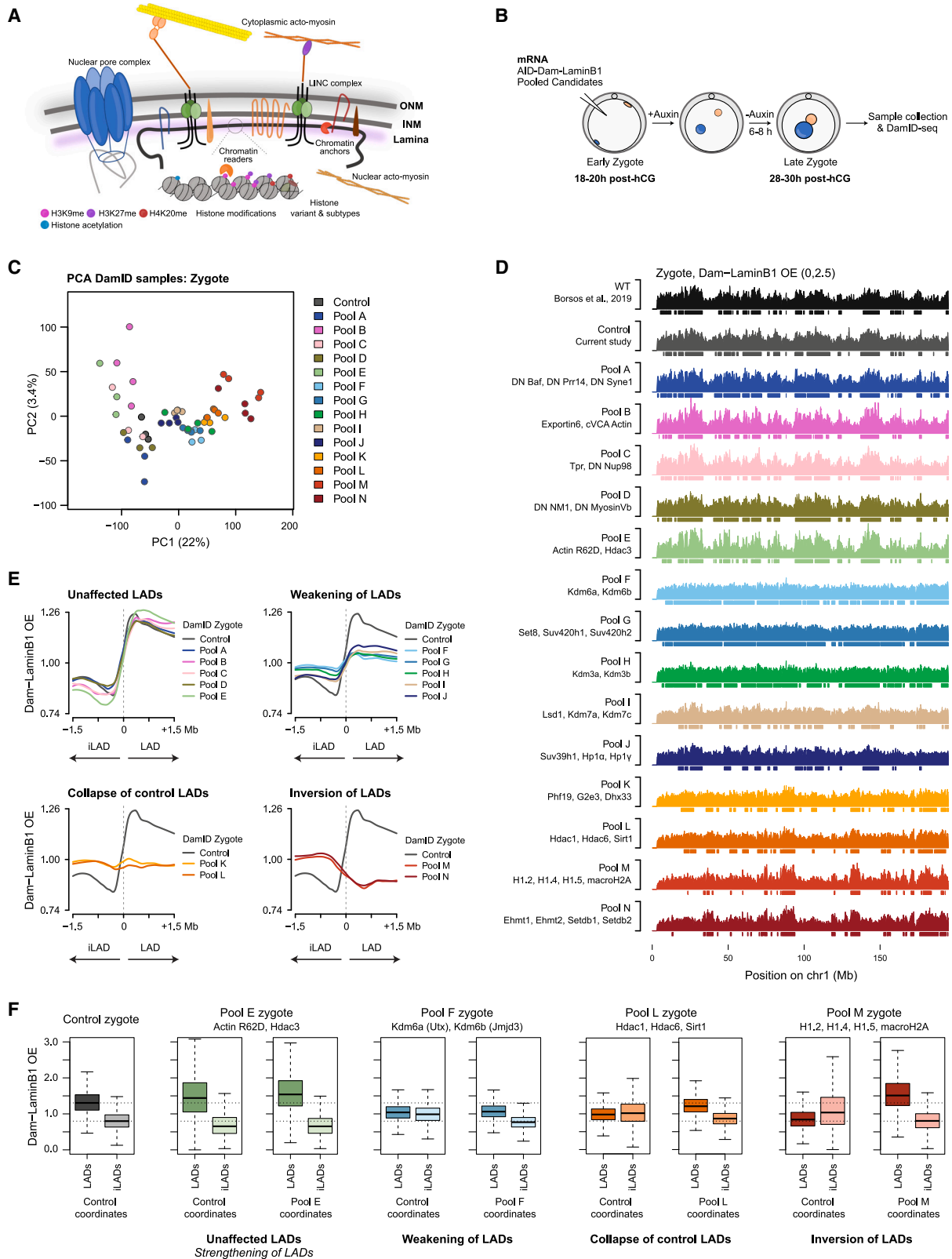
(legend on next page)

or constant iLADs. Thus, while significant LAD remodeling occurs during the subsequent developmental stages, almost half the genome acquires its "long-life" positioning immediately after fertilization. The H3K4 demethylase KDM5B affects LAD establishment in the paternal chromatin after fertilization,[24] and maternal H3K27me3 influences intercellular heterogeneity of genome-lamina interactions at the 2-cell stage.[26]

Here, we set out to investigate the epigenetic and structural components that influence LAD establishment in mouse embryos and their involvement in the LAD reorganization during MZT. We demonstrate that multiple chromatin pathways contribute to the integrity of LAD establishment and can influence nuclear organization at the time of zygotic genome activation (ZGA). Our data unveil that LAD establishment in zygotes is dispensable for early developmental progression. Instead, mouse embryos show a remarkable capacity to reset nuclear organization. Our work furthers our understanding of nuclear organization at the beginning of development.

RESULTS

Multiple phenotypes of disrupted nuclear organization emerge upon perturbation of chromatin and nuclear structural pathways after fertilization

To identify molecular determinants of LAD establishment *in vivo*, we performed a screen in mouse embryos, focusing on proteins involved in various nuclear processes, including histone modifiers, chromatin anchors, structural nuclear envelope proteins, and regulators of actomyosin (Figure 1A; Table S1). We devised a two-step screening strategy—first, with pooled candidates using gain-of-function or dominant-negative (DN) approaches (Figure S1A). The individual pool constituents are shown in Figure S1A and described in Table S1. As a readout, we mapped LADs using LaminB1-DamID.[24,27,28] For each pool of candidates, we performed mRNA microinjections into hybrid zygotes immediately after fertilization and collected DamID libraries of late zygotes (Figure 1B; Table S2). We verified the corresponding perturbations by immunostaining, including global changes in levels of the relevant histone modifications (Figure S1B). Principal-component analysis (PCA) identified candidate pools that deviated from control zygotes along PC1 or PC2 (Figure 1C). Pool B containing exportin6 and a membrane-tethered cortical actin nucleator that affects nuclear and cortical actin,[29,30] and pool M comprising histone variant macroH2A and H1 subtypes were located furthest from controls on PC2 and PC1, respectively. Additional candidate pools showed spreading along

PC1 away from the controls, albeit less pronounced (Figure 1C). To examine the candidate pools in detail, we called LADs using a two-state hidden Markov model (HMM) based on Dam-LaminB1 methylation levels.[27] We confirmed changes in nuclear positioning of selected LADs and iLADs by 3D-DNA fluorescence *in situ* hybridization (FISH) (Figure S1C). Visual inspection of chromosome tracks revealed highly similar LAD profiles between control samples and our previously mapped LADs in zygotes[24] (Figures 1C and 1D). Some candidate pools had no major LAD profile differences compared with controls, for example, upon expression of the DN nucleoporin 98[31] and nuclear pore component Tpr (pool C) (Figure 1D). However, several pools displayed severely impaired LAD profiles, including H3K27me3 demethylases (pool F) and H4K20 methyltransferases (pool G) (Figure 1D), which were associated with a strong increase in LAD size and the proportion of the genome associated with the lamina (Figures S1D and S1E). The latter could be because HMM fails to distinguish LADs/iLADs when the dynamic range of DamID observed over expected (OE) values is small. Another group displayed a phenotype with distinguishable LAD and iLADs but at different genomic locations than controls. These included the subtypes of H1 and histone macroH2A (pool M) and a histone deacetylase group (pool L) (Figure 1D), suggesting that manipulation of histone content in zygotic chromatin and/or of global acetylation results in LAD formation at aberrant genomic regions. Overall, the effects observed on LAD size and number varied across the tested pools (Figures S1D and S1E).

To further characterize the perturbations, we categorized phenotypes based on metaplots of LaminB1-DamID scores over control zygotic LAD boundaries (Figure 1E). This revealed four main patterns: (1) unchanged or strengthened LADs (increased Dam-LaminB1 methylation levels within LADs), (2) weakened LADs (decreased Dam-LaminB1 methylation levels within LADs), (3) collapse of control LADs (similar Dam-LaminB1 methylation levels between control LADs and iLADs), and (4) inversion of LAD architecture (control LADs become iLADs and vice versa) (Figure 1E). To investigate whether these phenotypes are due to restructured LAD boundaries, the emergence of new LADs, a change in the strength of interactions with the lamina, or a combination of these, we determined *de novo* LAD coordinates across our pools. We compared DamID scores in such *de novo* called LAD coordinates against control LAD coordinates (Figures 1F and S1F). Kdm6a/b (pool F) reduced lamina interactions of control LADs, leading to "weakened" LADs (Figure 1F). Such reduced interactions with the lamina were most pronounced for the pools that elicited LAD inversion (Figures 1F

Figure 1. Multiple phenotypes of disrupted nuclear organization emerge upon perturbation of chromatin and structural pathways after fertilization

(A) Schematic of targeted nuclear and chromatin features. ONM, outer nuclear membrane; IMM, inner nuclear membrane.

(B) Experimental design.

(C) Principal-component analysis (PCA) of phase I zygotic DamID samples. Each dot represents a biological replicate.

(D) Observed over expected (OE) Dam-LaminB1 mean values from biological replicates. Boxes represent LADs as per two-state HMM. Wild-type (WT) is published zygotic data (GEO: GSE112551) reanalyzed with the same pipeline. Candidates within pools are shown.

(E) Average OE values over control zygotic LAD boundaries. Zero and dotted lines indicate LAD/iLAD boundary.

(F) Boxplots of Dam-LaminB1 OE mean values in control and *de novo* called LAD/iLADs. Horizontal dotted lines indicate median OE values from control zygotic LADs (upper) and iLADs (lower).

See also Figure S1 and Tables S1 and S2.

Cell
Resource
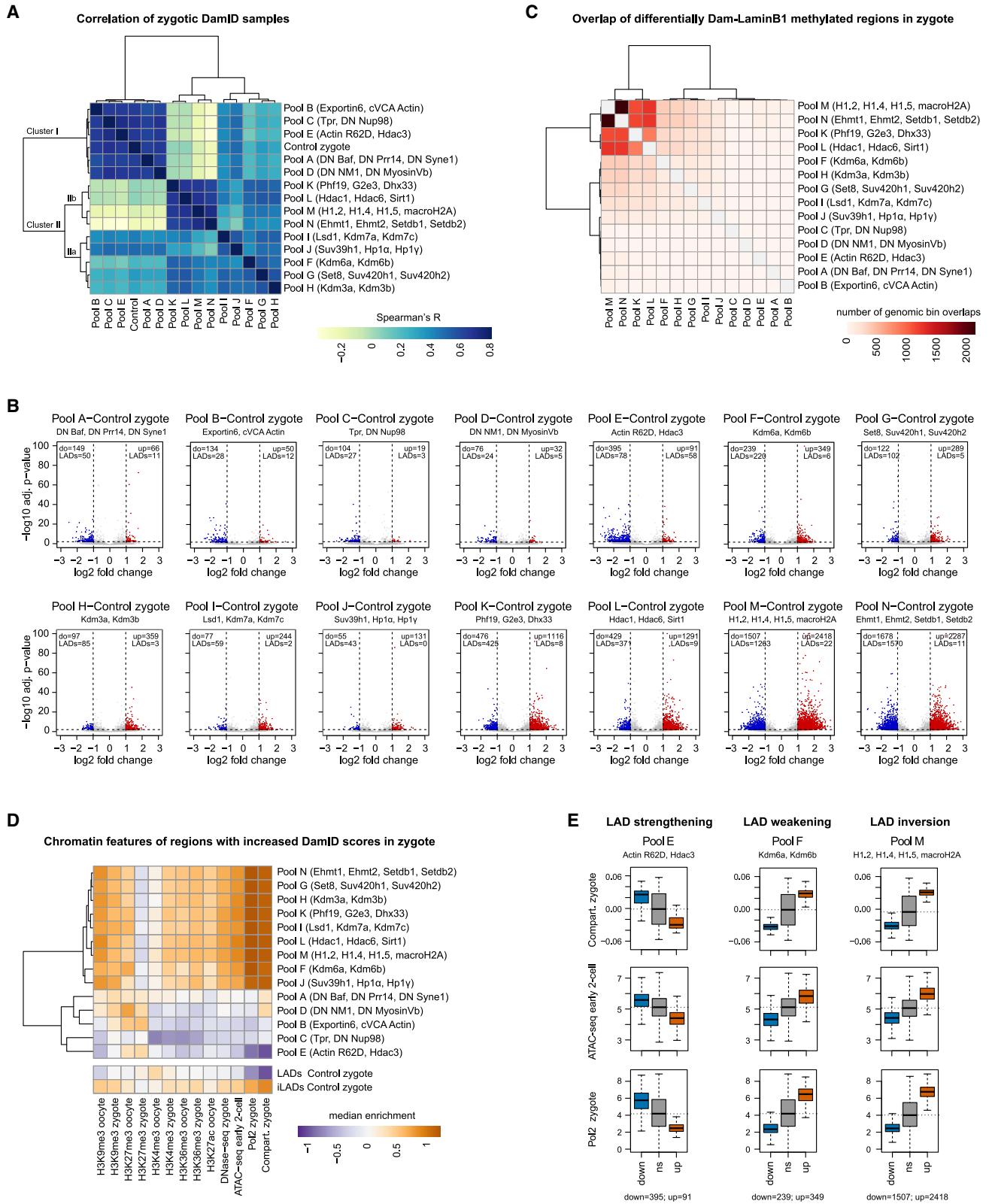
(legend on next page)

and S1F). This analysis also confirmed that LAD strengthening entails changes in DamID methylation levels within existing LADs and not a major global repositioning of genomic regions (pool E) (Figures 1F and S1G). This is potentially due to reduced nuclear size in zygotes from pool E (Figure S1H),[32] suggesting that nuclear size is important for increased strength of genome-lamina interactions.

Alluvial plots also highlight more widespread interchanges of genomic regions between LADs and iLADs in the inversion (pools M and N) (Figure S1G) compared with the collapse pools (pools K and L) (Figure S1G), indicating that collapse is an intermediate phenotype between control and LAD inversion. Specifically, conversion of LADs into iLADs occurs in pools K and L (collapse), but control LADs and iLADs have overall similar median DamID values (Figures 1F, S1F, and S1G). By contrast, median DamID values are inversed in pools M and N such that control iLADs have higher DamID values (Figures 1F and S1F). In general, most perturbations affect both maternal and paternal pronuclei (Figure S1I). For instance, LADs were inverted in both alleles for those pathways associated with LAD inversion (pool N) (Figure S1J). However, in some cases, we observed differential effects, consistent with the differences in epigenetic features between the two parental chromatins at these early stages. For example, this was observed in zygotes where the H4K20 pathway was targeted (pool G) or upon expression of H3K9me2 demethylases (Kdm3a/b, pool H) (Figures S1I and S1J). Thus, our phase I screening recovered multiple phenotypes of disrupted nuclear organization, suggesting the involvement of different players in establishing zygotic nuclear architecture.

Chromatin features associated with disrupted LAD establishment

To gain further insight into the principles governing zygotic genome organization, we analyzed genome-wide correlations of LaminB1-DamID scores across all tested conditions (Figure 2A). This revealed two major clusters, which largely coincided with the phenotypes described above. The first major cluster (cluster I) contained zygotes in which genome-lamina interactions remained globally unaffected or became stronger (Figure 2A). The second major cluster (cluster II) included the perturbations that led to the disruption of control LADs (Figure 2A). Clusters I and II were defined by candidates targeting the nuclear envelope or cytoskeleton and heterochromatin manipulation, respectively. Cluster II further subdivided into two: IIa with weaker LAD interactions with the lamina, such as Kdm6a/b (pool F), Kdm3a/b (pool H), Lsd1 and Kdm7a/c (pool I), and IIb,

which included the pathways leading to collapsed (pools K and L) or inverted LAD architecture (pools M and N) (Figure 2A).

Next, we asked about the impact of various perturbations at a genome-wide scale. We extracted genomic bins displaying significantly higher and lower LaminB1-DamID scores upon perturbation (Figure 2B; Table S3). Perturbing histone content (pool M) or expressing H3K9 methyltransferases Ehmt1/2 and Setdb1/2 (pool N) had the highest number of bins affected (Figure 2B). Upon expression of histone H1 subtypes and macroH2A (pool M), 2,418 bins gained interaction with the lamina. Of these, only 22 correspond to control LADs, while 2,396 correspond to iLADs (Figure 2B), highlighting LAD inversion. We observed a high overlap of affected bins among pools belonging to cluster IIb (Figure 2C, top left corner). This group consisted of pools K, L, M, and N, which target very different processes (Figure 2C). This trend was similar for regions that lost interactions with the lamina (Figures S2A and S2B). These observations suggest that the same regions are affected even when disruption is caused by different pathways.

Overall, perturbing chromatin pathways increased nuclear lamina association of regions in wild-type A compartments, which exhibit strong RNA polymerase II (RNA Pol II) occupancy and higher accessibility (Figures 2D and 2E). In other words, perturbation of all tested chromatin pathways led to increased lamina interactions of control iLADs. By contrast, disrupting structural components of the nuclear membrane, anchor proteins, and actomyosin led to increased lamina association of regions depleted of RNA Pol II and lacking clear compartment association (Figure 2D). An exception was perturbation of nuclear actin polymerization (pool E), where increased lamina interactions occurred at B-compartment regions (Figures 2D and 2E). Analysis of the regions that lost interactions with the lamina upon perturbation led to a similar clustering pattern (Figure S2C). Additionally, in all chromatin modifier perturbations, maternally marked H3K27me3 regions that lose H3K27me3 after fertilization gain lamina interactions (Figure 2D), suggesting a role of specific chromatin feature(s) in regulating lamina association.

Identification of pathways that regulate LAD reorganization after the first mitotic division

Next, we searched for factors that alter LAD remodeling during MZT, which occurs by the late 2-cell stage.[24] We performed a new phase I screening at the late 2-cell stage using an auxin degron to temporally control DamID[24] (Figure 3A; Table S2). We confirmed the perturbation of the respective molecular pathway by immunostaining (Figure S3A) and were able to evaluate the impact of all pooled perturbations, except for nuclear export

---

Figure 2. Integration of nuclear organization phenotypes reveals chromatin features associated with disrupted LAD establishment
(A) Hierarchical clustering and genome-wide Spearman's R of Dam-LaminB1 OE mean values.
(B) Volcano plots showing genomic regions with significantly higher ("up", red dots) or lower ("do"; down, blue dots) OE values. The number of up/do genomic bins that belong to LADs in control zygotes is indicated.
(C) Heatmap showing overlap of all genomic regions with differential lamina interactions (up + do) with respect to controls.
(D) Enrichment of wild-type chromatin features in up genomic regions. Chromatin feature enrichment in control zygotic LADs/iLADs is shown for comparison. Positive compartment scores (Compart.) define A-compartment.
(E) Boxplots showing compartment score, chromatin accessibility, and RNA Pol II occupancy in up or down regions. The horizontal dotted lines indicate the median signal in the "ns" (non-significant) genomic regions.
See also Figure S2 and Table S3.
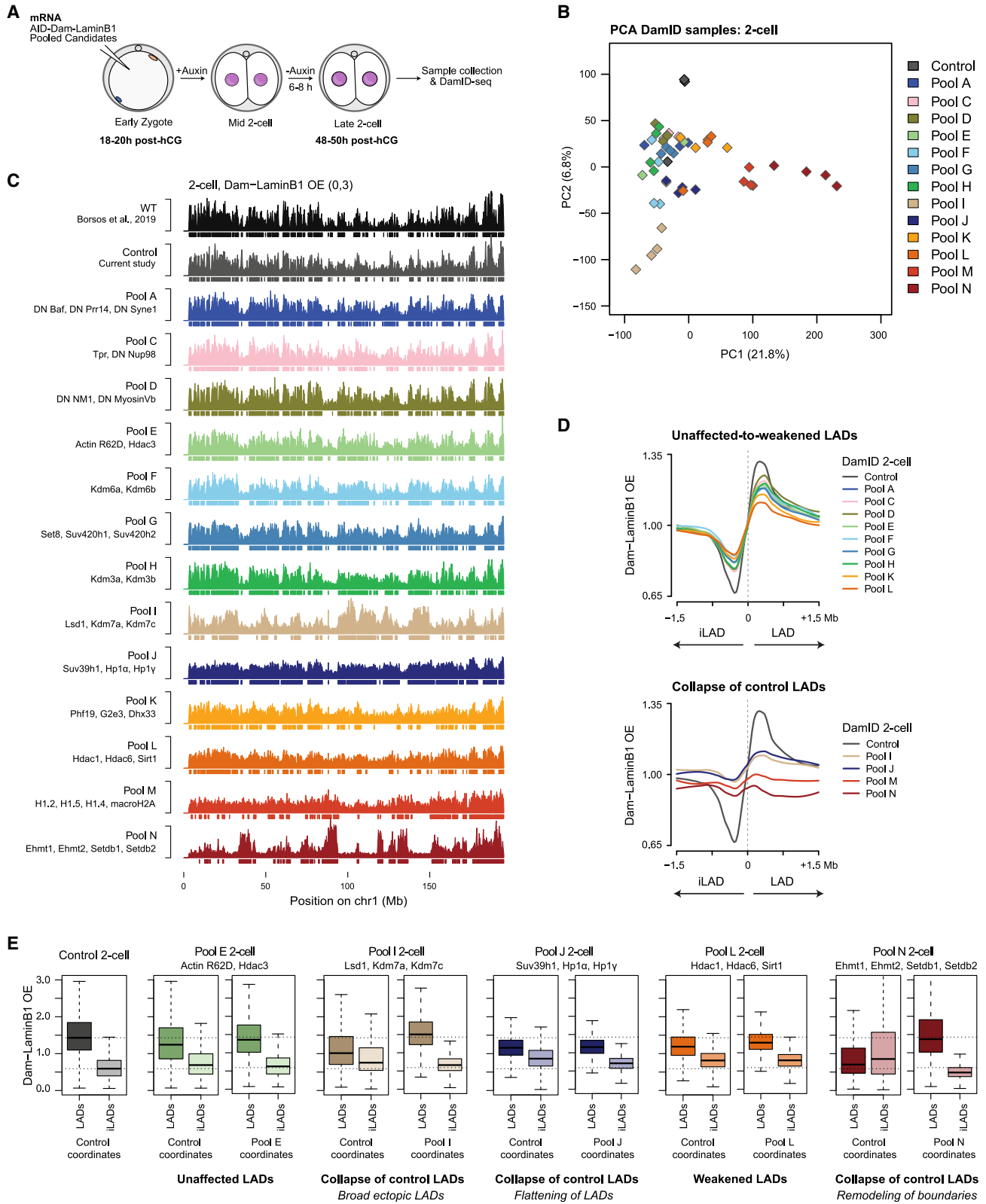
Cell
Resource

(legend on next page)

and cortical actin dynamics (pool B) because they blocked the completion of cytokinesis prior to the 2-cell stage.[29] In general, most samples did not deviate from controls on the PCA (Figure 3B). Exceptions were 2-cell embryos expressing: (1) the H3K4me2 demethylase Lsd1 with the H3K9me2/K27me2 demethylases Kdm7a/c (pool I), (2) the H3K9me2/me3 methyltransferases Ehmt1/2 and Setdb1/2 (pool N), and (3) the histone H1 subtypes and macroH2A (pool M) (Figure 3B).

We applied HMM to determine LADs and confirmed changes in nuclear positioning of selected LADs and iLADs by 3D-DNA FISH (Figure S3B). Visualizing DamID scores within LADs/iLADs revealed, in general, more subtle changes in LAD structure compared with the same perturbations in zygotes (Figure 3C vs. Figure 1D), with a notable exception for the perturbation in the H3K9me2/me3 "writer" pathway (Figure 3C, pool N). LAD number was also affected, ranging from 278 (Suv39h1 and Hp1α/γ; pool J) to 646 (DN Nup98 and Tpr; pool C) compared with 831 in controls (Figure S3C). This was accompanied by changes in LAD size and in the proportion of the genome associated with the lamina (Figures S3C and S3D).

Next, we categorized 2-cell-stage phenotypes based on metaplot profiles. Piling-up LaminB1-DamID scores over control LAD boundaries revealed two major phenotypes with different levels of perturbation: (1) unaffected-to-weaker LAD/iLAD distinction with a globally preserved wild-type LAD structure (decreased Dam-LaminB1 methylation levels within control LADs) and (2) collapse of control LAD architecture (overall similar Dam-LaminB1 methylation levels between control LADs and iLADs) (Figure 3D). Most tested pools are in the unaffected-to-weaker group. However, manipulating constitutive heterochromatin pathway (pool J), the expression of the H3K4me2, H3K9me2/K27me2 demethylases Lsd1 and Kdm7a/c (pool I), H3K9me2/3 methyltransferases Ehmt1/2 and Setdb1/2 (pool N), and the histone H1 subtypes/macroH2A (pool M) led to a profound alteration of DamID values across the control 2-cell-stage LAD boundaries (Figure 3D, bottom).
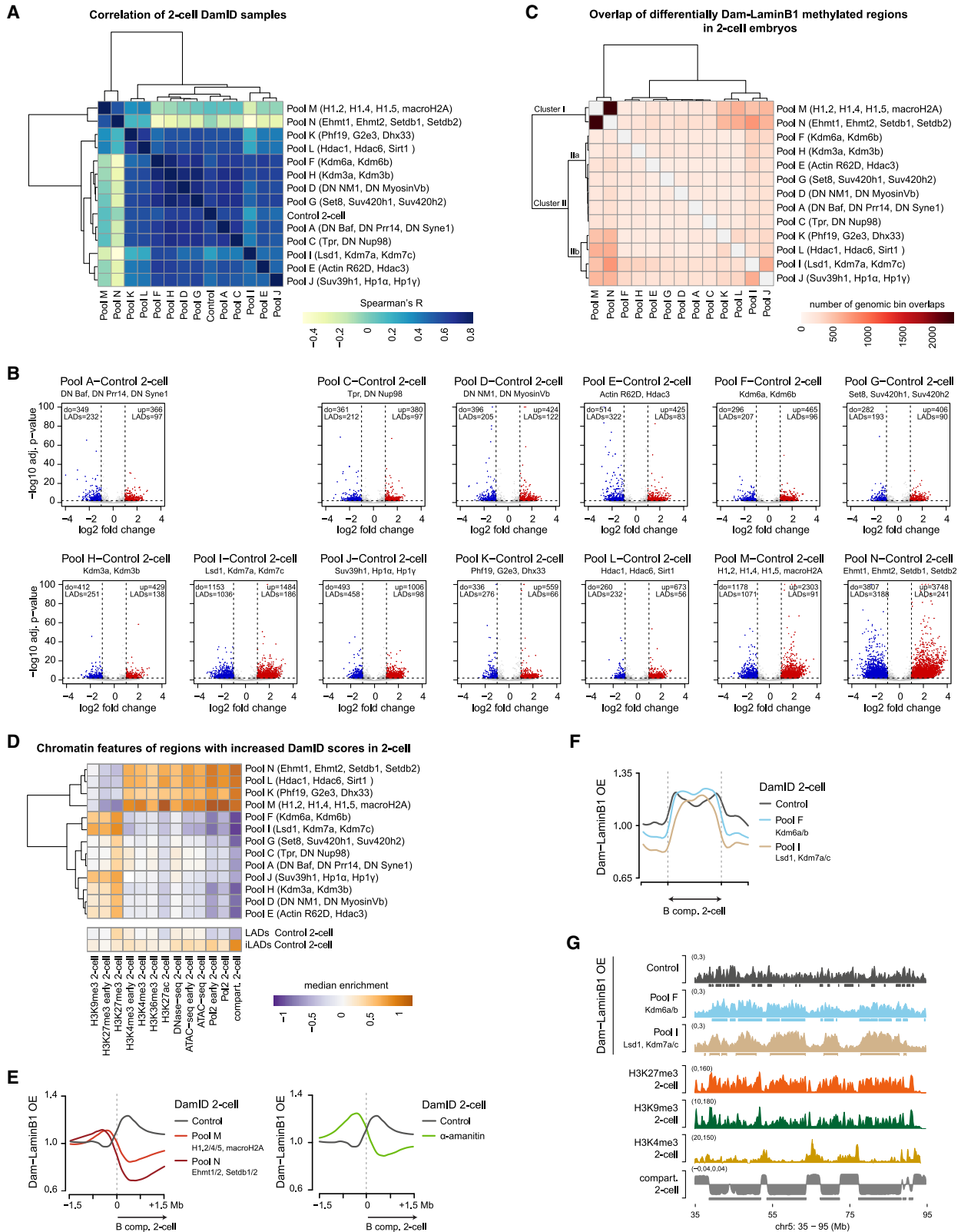
Plotting genome-wide LaminB1-DamID scores against *de novo* called LADs, which we calculated using HMM for each pool, confirmed that control LAD structure was largely preserved in most pools (pools A–H, K, and L) (Figures 3E and S3E). Among the strongest 2-cell-stage phenotypes, the constitutive heterochromatin pathway (pool J) led to LAD flattening (Figures 3C and 3D) resulting from less distinct DamID methylation levels between LADs and iLADs (Figure 3E). By contrast, global perturbation of H3K4me2 and H3K9me2/K27me2 with Lsd1 and Kdm7a/c (pool I) leads to ectopic expansion of some LADs beyond their normal boundaries (Figure 3C), resulting in an apparent collapse

of control LADs (Figure 3D) and a reduction in the relative DamID values between control LADs and iLADs (Figure 3E). Remarkably, expression of the H3K9me2/me3 writers Ehmt1/2 and Setdb1/2 (pool N) led to the collapse of control 2-cell-stage LADs through yet another process: a strong decrease of DamID scores in wild-type LADs (Figure 3E). However, they still displayed a clear LAD-iLAD structure, with distinct DamID values between *de novo* called LADs and iLADs (pool N) (Figure 3E), indicating that LAD boundaries reposition upon H3K9me2/me3 writers' expression. The collapse of control LADs upon expression of histone H1 subtypes and macroH2A (pool M) stemmed from a similar remodeling of LAD boundaries (Figures 3C, 3D, and S3E). We detected enrichment of the tagged histones that we expressed in the nuclear periphery (Figure S3F). Global H3K9me2 levels increased in pool N as expected but not in pool M (Figure S3G). Thus, similar LAD phenotypes do not necessarily stem from perturbing the same histone modifications. Overall, our data suggest that H3K4, H3K9, and/or H3K27 methylation pathways are involved in the correct positioning of LAD boundaries at the 2-cell stage.

Next, we asked whether pathways regulating LAD establishment in zygotes also affect LAD reorganization at the 2-cell stage. First, combining all samples into one PCA revealed that embryos broadly grouped according to their developmental stage, regardless of the perturbation (Figure S3H). An exception was 2-cell embryos expressing the H3K4me2 and H3K9me2/K27me2 demethylases Lsd1 and Kdm7a/c (pool I), which clustered with zygotes (Figure S3H). Second, we compared *de novo* called LADs and iLADs upon perturbation to LADs and iLADs in control zygotes and 2-cell embryos (Figure S3I). While LAD formation was disrupted in zygotes by several pathways, the affected genomic regions regained their overall LAD/iLAD wild-type structure at the 2-cell stage (pools F, G, H, K, and L) (Figure S3I). Such a "recovery" phenotype was striking: for example, perturbing histone acetylation led to a collapse of control zygotic LADs, but only to a minor phenotype at the 2-cell stage (pool L) (Figure S3I). This was not due to the lack of perturbation of the targeted histone modification(s), as the respective modifications were affected in embryos where LAD architecture was unaffected at the 2-cell stage (pools F, G, H, and L) (Figure S3A). Because expression of the pooled candidates occurs continuously, from early zygote to 2-cell stage, we conclude that nuclear organization in zygotes is highly adaptive and that even strong perturbations of LADs in the zygote can be reset to conditions similar to wild-type in the next cell cycle. Thus, while interactions established after fertilization in the zygote may contribute to the definition of the nuclear organization at

Figure 3. Identification of pathways that regulate LAD reorganization after the first mitotic division

(A) Experimental design. Microinjections are performed immediately after fertilization (18–20 h post-human chorionic gonadotropin [hCG]), and therefore candidates are expressed from zygote stage.

(B) PCA of 2-cell DamID samples from phase I screening. Each dot represents a biological replicate.

(C) 2-cell Dam-LaminB1 OE mean values on chromosome1. Boxes represent LADs called using two-state HMM. Previous 2-cell data (GEO: GSE112551) re-analyzed with the same pipeline is shown as wild-type (WT) for comparison.

(D) Average Dam-LaminB1 OE value over control 2-cell LAD boundaries. Zero and dotted lines indicate LAD/iLAD boundary.

(E) Boxplots of Dam-LaminB1 OE mean values in control and *de novo* called LAD/iLADs. Horizontal dotted lines indicate median OE values from control 2-cell LADs (upper) and iLADs (lower).

See also Figure S3 and Table S2.

A Correlation of 2-cell DamID samples

B

Pool A−Control 2-cell — DN Baf, DN Prr14, DN Syne1
Pool C−Control 2-cell — Tpr, DN Nup98
Pool D−Control 2-cell — DN NM1, DN MyosinVb
Pool E−Control 2-cell — Actin R62D, Hdac3
Pool F−Control 2-cell — Kdm6a, Kdm6b
Pool G−Control 2-cell — Set8, Suv420h1, Suv420h2
Pool H−Control 2-cell — Kdm3a, Kdm3b
Pool I−Control 2-cell — Lsd1, Kdm7a, Kdm7c
Pool J−Control 2-cell — Suv39h1, Hp1α, Hp1γ
Pool K−Control 2-cell — Phf19, G2e3, Dhx33
Pool L−Control 2-cell — Hdac1, Hdac6, Sirt1
Pool M−Control 2-cell — H1.2, H1.4, H1.5, macroH2A
Pool N−Control 2-cell — Ehmt1, Ehmt2, Setdb1, Setdb2

C Overlap of differentially Dam-LaminB1 methylated regions in 2-cell embryos

D Chromatin features of regions with increased DamID scores in 2-cell

E DamID 2-cell

F DamID 2-cell

G Dam-LaminB1 OE

(legend on next page)

Cell
Resource

CellPress
OPEN ACCESS

the 2-cell stage, embryos at the 2-cell stage can reestablish LADs *de novo* when nuclear organization is not correctly initiated in zygotes.

Disrupting histone methylation pathways reshapes LAD boundaries at the 2-cell stage

Genome-wide correlation analyses of LaminB1-DamID values resulted in two primary clusters, separating 2-cell embryos with perturbation of H3K9me2/me3 writers and histone H1 subtypes and macroH2A (pools N and M) from the remainder (Figure 4A). Globally, all candidate pools tested led some regions to reposition toward the nuclear lamina (gained Dam-LaminB1 methylation levels) or toward the interior (lost Dam-LaminB1 methylation levels) (Figure 4B; Table S4). The number of bins with differential Dam-LaminB1 methylation varied, with most pools leading to only minor changes (pools A–H). The H3K9 methyltransferases Ehmt1/2 and Setdb1/2 showed the strongest phenotype (7,555 bins affected; pool N) (Figure 4B). A large number of bins that are iLADs in control 2-cell embryos gained lamina interactions in pools M and N (2,212 and 3,507, respectively) (Figure 4B), suggesting a partial inversion phenotype.

Analysis of the overlap in the genomic regions affected revealed two major clusters (Figure 4C) with an overall similar structure regardless of whether they gained or lost lamina interactions (Figures S4A and S4B). The pools with the strongest control LAD collapse phenotype (cluster I) separated from the main cluster (cluster II) (Figure 4C). Cluster I comprised the H3K9me2/me3 writers (pool N) and histone subtypes/variants (pool M). Within cluster II, a secondary cluster (cluster IIa) contained a group of milder phenotypes (pools A–H) (Figure 4C), while cluster IIb included four pools targeting different pathways with either collapse or unaffected-to-weakened phenotypes (pools I–L). A distinct pattern of chromatin features characterized genomic regions that gained lamina interactions at the 2-cell stage. The strongest association was with their compartment score in control embryos (Figures 4D and S4C). H3K9me writers, histone deacetylases, and histone subtypes/variants direct the repositioning of euchromatic A-compartment regions toward the lamina. On the other hand, B-compartment regions marked by H3K27me3 and H3K9me3 gained lamina interactions upon perturbations such as the constitutive heterochromatin pool (pool J) (Figure 4D).

We asked whether LAD phenotypes from chromatin modifiers relate to ZGA by comparing them with α-amanitin-treated late 2-cell-stage embryos.[25] We observed extensive overlap between regions that significantly change lamina interactions upon α-amanitin treatment and those affected upon expression of histone H1 subtypes and macroH2A (pool M) and the H3K9me2/me3 methyltransferases Ehmt1/2 and Setdb1/2 (pool N) (Table S4; Figure S4D). Notably, *de novo* LAD boundaries upon transcriptional inhibition or chromatin perturbations that lead to the collapse of LADs remain within A/B compartment boundaries (Figure 4E), suggesting that compartment boundaries provide a primary scaffolding cue to genome organization at the beginning of development.

We next investigated LAD regulation by H3K27 and H3K9 methylation at compartment boundaries. Co-expression of Kdm6a and Kdm6b increased lamina interactions of regions inside B compartments and led to stronger demarcation of DamID score at compartment boundaries (pool F) (Figure 4F). We obtained similar results upon expression of H3K4me2 and H3K9me2/K27me2 demethylases Lsd1 and Kdm7a/c (pool I) (Figure 4F), which lowered the average DamID scores in A-compartment regions. Expression of Kdm6a/b (pool F) led to the fusion of LADs along regions enriched in H3K27me3 (and H3K9me3) that did not extend beyond regions demarcated by H3K4me3 domains (Figure 4G). We obtained similar results with Lsd1 and Kdm7a/c expression (pool I), with larger, more defined LADs overall covering complete H3K27me3 domains, although the "merging" phenotype was stronger compared with Kdm6a/b (Figure 4G). Thus, we conclude that the interplay between H3K9, H3K27, and H3K4 methylation is a major determinant of LAD reorganization and boundary positioning during MZT at the 2-cell stage.

Identification and characterization of individual effectors that regulate the establishment of LADs after fertilization and during MZT

To gain further insights into the processes underpinning early genome organization, we focused on the pools that conferred the strongest phenotypes: the constitutive heterochromatin pathway (pool J), the H3K9me2/me3 methyltransferases (pool N), and the H3K4me2 and H3K9me2/K27me2 demethylases (pool I). We assessed the effects of expressing 10 individual chromatin modifiers and readers on LAD establishment (Suv39h1, Ehmt1, Ehmt2, Setdb1, Setdb2, Lsd1, Kdm7a, Kdm7c, Hp1α, and Hp1γ). We mapped LADs in zygotes as above (Figure 5A; Table S5) and verified that efficient nuclear

Figure 4. Disrupting histone methylation pathways leads to remodeling of LAD boundaries at the 2-cell stage with altered concordance with compartments

(A) Hierarchical clustering and genome-wide Spearman's R correlation of OE mean values.

(B) Volcano plots showing genomic regions with significantly higher (up, red dots) or lower (do; down, blue dots) OE values. The number of up/do genomic bins that belong to LADs in control 2-cell embryos is indicated.

(C) Heatmap showing overlap of all genomic regions with differential lamina interactions (up + do) with respect to controls.

(D) Enrichment of wild-type chromatin features in up genomic regions. Chromatin feature enrichment in control 2-cell LADs/iLADs is shown for comparison. Positive compartment scores (Compart.) define A-compartment.

(E) Metaplots of average Dam-LaminB1 OE value over control 2-cell A/B compartment boundaries. Data from α-amanitin-treated 2-cell embryos, GEO: GSE241483.

(F) Metaplot showing average Dam-LaminB1 OE value over scaled B-compartment regions in 2-cell embryos.

(G) Dam-LaminB1 OE value, histone modification enrichment, and compartment score from 2-cell embryos visualized on part of chromosome5. Boxes below OE value tracks depict LADs, and wild-type 2-cell B compartments are indicated.

See also Figure S4 and Table S4.
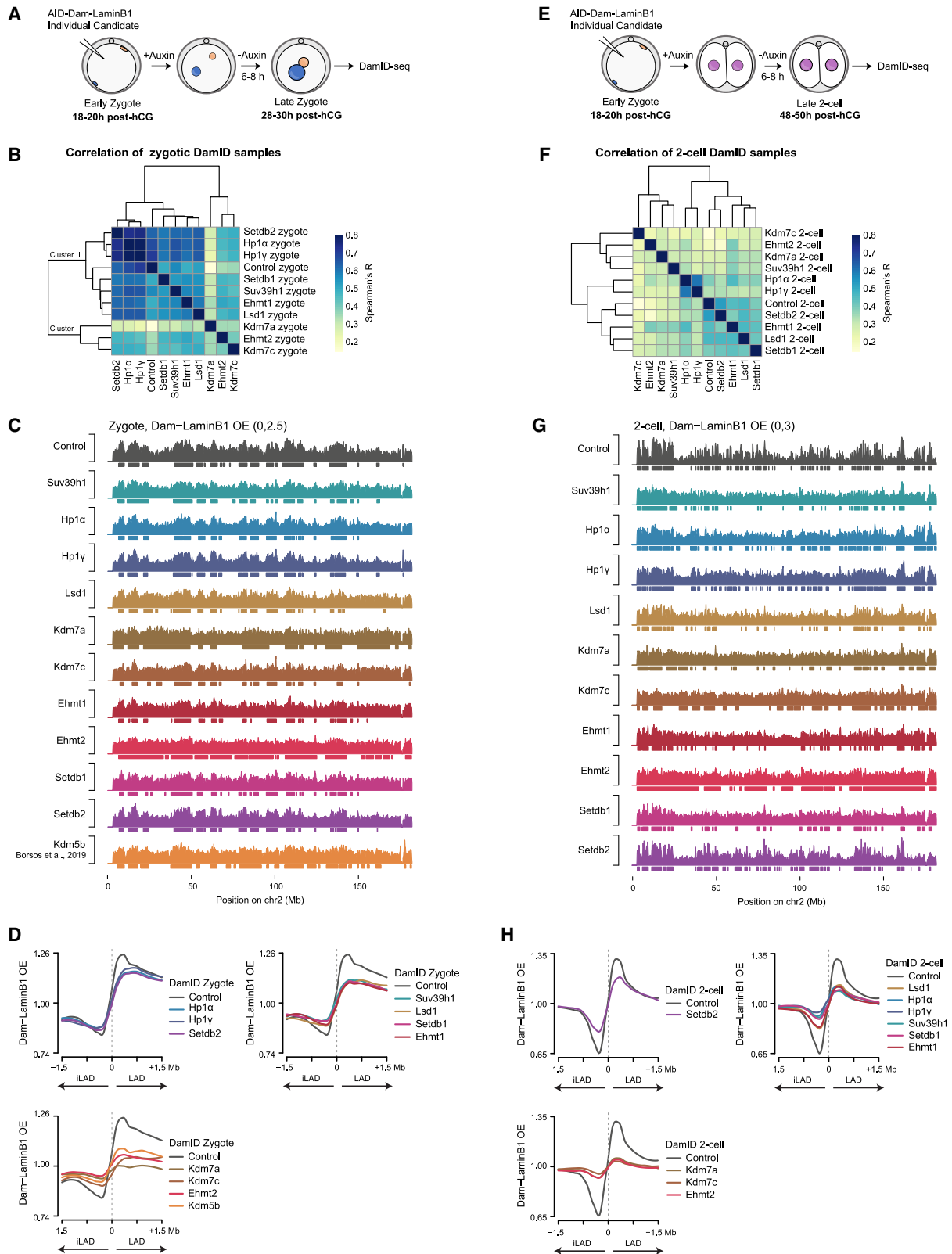
(legend on next page)

expression of each protein persists until the 2-cell stage (Figure S5A). Genome-wide correlation analysis of LaminB1-DamID indicated that the perturbed zygote samples globally clustered together, suggesting similar phenotypes, except for zygotes expressing the Kdm7a or Kdm7c demethylases and the Ehmt2 methyltransferase (cluster I), from the rest (cluster II) (Figure 5B). Zygotic LADs were highly disrupted by Kdm7a, Ehmt2, and Kdm7c (Figure 5C). LAD size and the proportion of the genome assigned to the lamina were particularly affected by Ehmt2 and Kdm7a expression (Figures S5B and S5C). The changes caused by these two modifiers were more pronounced than those caused by the H3K4me3 demethylase Kdm5b expression[24] (Figures 5C, S5B, and S5C).

Plotting LaminB1-DamID scores across control LAD boundaries confirmed that the strongest phenotypes were caused by Kdm7a, Kdm7c, and Ehmt2, along with Kdm5b, all showing flattening of wild-type LADs (Figure 5D). While zygotes expressing Kdm7a do not have distinguishable DamID methylation levels between control LADs and iLADs, they do have a clear distinction of DamID methylation between *de novo* LADs and iLADs (Figure S5D). Zygotes expressing Ehmt2 and Kdm7c retain different DamID methylation levels between control LADs and iLADs, but the difference in DamID values is larger between *de novo* LADs and iLADs (Figure S5D). Expression of all other candidates did not affect overall wild-type LAD structure (Hp1α, Hp1γ, and Setdb2) or only caused weakening of control LADs (Suv39h1, Lsd1, Setdb1, and Ehmt1) (Figures 5D and S5D). We conclude that methylation of H3K9 and H3K27 is key for the organization of LAD boundaries in zygotes.

Next, we determined the effect of expressing the same 10 individual chromatin effectors at the late 2-cell stage (Figure 5E; Table S5). Ehmt2 displayed the strongest phenotype of LAD disruption in 2-cell embryos, along with Kdm7a and Kdm7c (Figures 5F–5H). Ehmt2 also induced changes in LAD size, number, and genome percentage at the lamina (Figures S5E and S5F). Lsd1, Setdb1, Suv39h1, and Ehmt1 reduced the difference between DamID values of control LADs and iLADs (Figure 5H) due to increased interactions of control iLADs with the lamina and reduced interactions of control LADs (Figures 5H and S5G). Additionally, Ehmt2 prevented the natural reorganization of LADs/iLADs that occurs between the zygote and the 2-cell stage (Figure S5H). Overall, methyltransferase activities toward H3K9me2/me3 and demethylation of H3K9me2 and/or H3K27me2 affect both the initial establishment of nuclear organization and the LAD reorganization during the 2-cell stage.

Individual effectors contribute to LAD establishment and reorganization in a non-redundant manner

We next examined the impact of specific candidates on euchromatic versus heterochromatic regions (Figure S6A; Table S6). Expression of heterochromatin readers Hp1α or Hp1γ displayed few bins that changed lamina interactions in zygotes (*n* = 31 and 29, respectively). However, both proteins had a stronger phenotype at the 2-cell stage (*n* = 1,778 and 1,909) (Figure S6A), suggesting that heterochromatin readers may have a stronger influence in positioning the genome at the 2-cell stage. Except for Hp1γ, all chromatin modifiers led to increased nuclear lamina association of strong A-compartment regions in zygote (Figure 6A). Expression of Suv39h1 and Setdb2 similarly affected A-compartment regions without a particular enrichment in active histone modifications but marked by H3K9me3 (Figure 6A). Analysis of the regions that reduced and/or lost interactions with the nuclear lamina revealed a roughly opposite pattern (Figure S6B). A similar analysis in 2-cell embryos indicated that Setdb1, Ehmt1, Ehmt2, Suv39h1, and Hp1α increased lamina interactions of A-compartment regions enriched in active chromatin marks (Figure 6B), suggesting that ectopic heterochromatin spreading promotes aberrant interactions with the lamina. Kdm7a and Kdm7c, involved in heterochromatin regulation, also displayed a similar pattern (Figure 6B).

For pool J, containing Suv39h1 and Hp1α/γ, we find that the strong disruption caused by the pool in zygotes was mostly recapitulated by Suv39h1 alone (Figure 6C). By contrast, at the 2-cell stage, Hp1α or Hp1γ could individually weaken control LADs to a level comparable to the pool (Figure 6D). We next computed H3K9me3 levels within regions affected by the constitutive heterochromatin pool and its individual components. In zygotes, regions that increase interactions with the lamina have higher H3K9me3 levels compared with non-affected regions or those relocating toward the interior (Figure S6D). By contrast, in 2-cell embryos, regions repositioning toward the lamina in response to pool J, Hp1α, or Hp1γ had higher H3K9me3 levels than those affected by Suv39h1 alone (Figure S6E). This effect is particularly evident for Hp1γ, whose expression leads to the formation of larger LADs over H3K9me3-marked regions (Figure S6F). These findings suggest that, at the 2-cell stage, LAD regulation is more influenced by chromatin readers and/or pre-existing H3K9me3-marked regions, in line with the progressive increase in H3K9me3 levels during development.[33,34]

Neither of the H3K9me2/me3 methyltransferases Ehmt1, Ehmt2, Setdb1, or Setdb2 alone recapitulated the extent of their

---

Figure 5. Identification and characterization of individual effectors that regulate the establishment of LADs after fertilization and their dynamics during MZT

(A) Experimental design for phase II zygote samples (e.g., individual modifiers).

(B) Hierarchical clustering and genome-wide Spearman's R correlation of Dam-LaminB1 OE mean values of zygotic samples.

(C) Zygotic Dam-LaminB1 OE mean values over chromosome2. Boxes represent LADs called by a two-state HMM. DamID data from zygotes expressing Kdm5b, GEO: GSE112551.

(D) Metaplot of Dam-LaminB1 OE value over control zygotic LAD boundaries. Zero and dotted lines indicate the LAD/iLAD boundary.

(E) Experimental design for 2-cell samples. Microinjections are performed immediately after fertilization (18–20 h post-hCG), and therefore candidates are expressed from zygote stage.

(F) Spearman's R correlation of genome-wide OE mean values between 2-cell samples.

(G) Dam-LaminB1 OE mean values at the 2-cell stage over chromosome2. Boxes below represent LADs.

(H) Average OE value over LAD boundaries of control 2-cell embryos.

See also Figure S5 and Table S5.
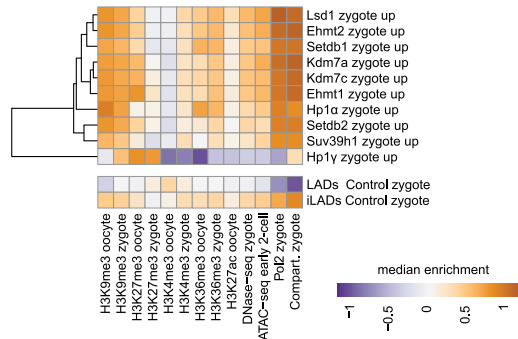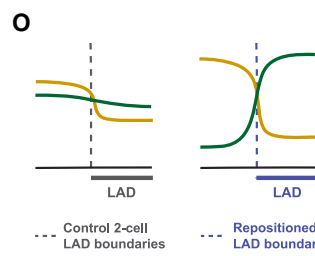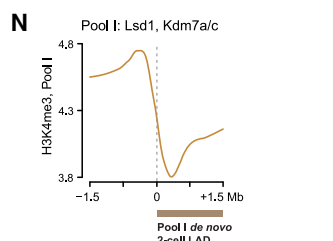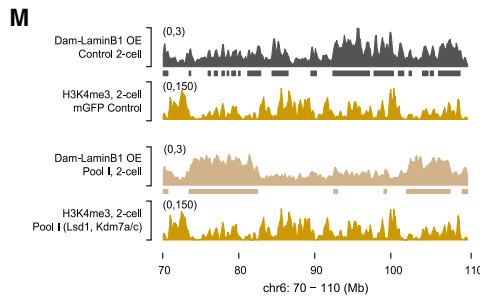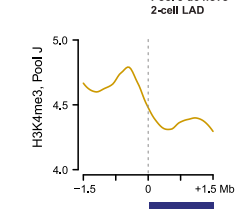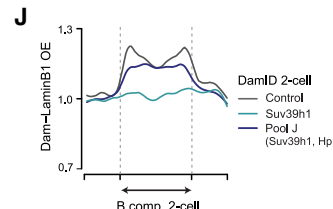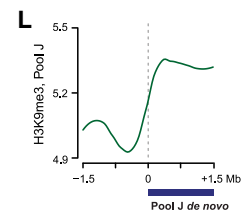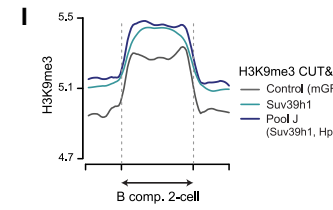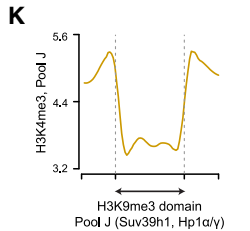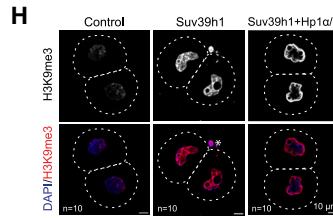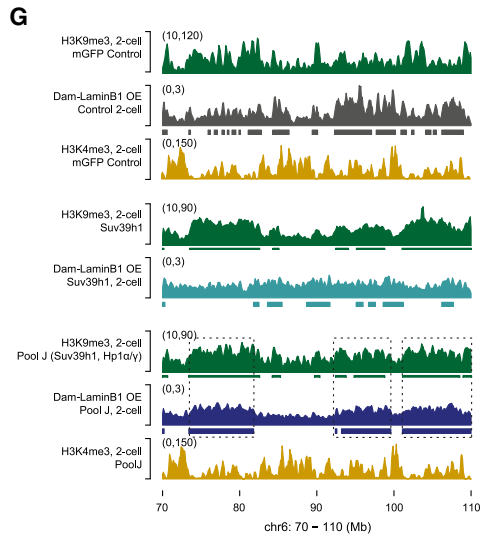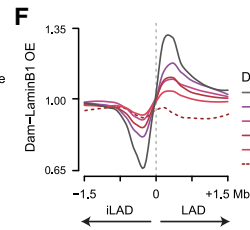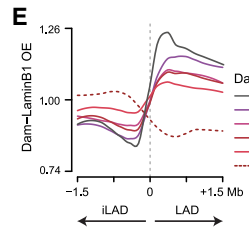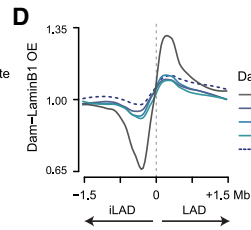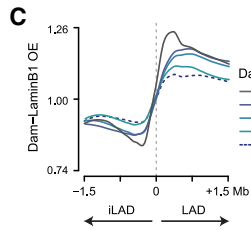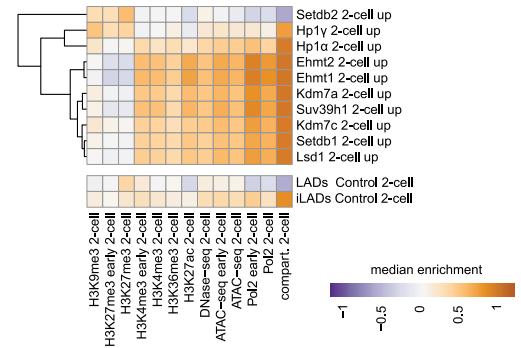
(legend on next page)

combined effect on LAD disruption (Figures 6E and 6F). Similarly for the H3K4me2 demethylase Lsd1. Individually, only Kdm7a or Kdm7c affect wild-type LAD structure in both zygotes and 2-cell embryos (Figures S6G–S6I), indicating that combined with H3K4me2 depletion, removal of H3K9me2/K27me2 can regulate LAD reorganization differently. These results imply that individual effectors within the chromatin pathways tested are non-redundant within the given pathway. Our findings suggest that LAD structuring is robust during development, and altering a single modulator is less likely to fully disrupt nuclear organization than manipulating multiple proteins within a pathway.

LAD boundaries reorganize based on positional information of H3K9me3 and H3K4me3 domains

We next aimed to gain further insights into LAD positioning by performing histone modification profiling under conditions where LAD boundaries are displaced. We focused on the constitutive heterochromatin pool (pool J), where LADs expand beyond control LAD boundaries (Figures 3C and S6F). We first asked if LAD expansion is linked to the acquisition of H3K9me3. CUT&RUN for H3K9me3 (Figure S6J) indicated combined expression of Suv39h1 and Hp1α/γ leads to broad H3K9me3 domains that reposition toward the lamina (Figure 6G), also visible by immunostaining (Figure 6H). Profiling H3K9me3 in Suv39h1-expressing 2-cell embryos revealed that while H3K9me3 expands into broad domains within B compartments beyond control LADs (Figures 6G and 6I), these domains do not necessarily relocate to the lamina (Figures 6G and 6J). Thus, H3K9me3 alone is not sufficient to drive stable interactions with the lamina. The above findings suggest that the interplay of H3K9me3, H3K27me2/3, and H3K4me3 may be a determinant for LAD reorganization at the 2-cell stage and the potential role of euchromatin in counteracting heterochromatin spreading. Therefore, we profiled H3K4me3 in embryos from pool J using CUT&Tag (Figure S6K). H3K4me3 levels are largely unchanged upon expression of the constitutive heterochromatin pool (Figure S6L). However, ectopic H3K9me3 domains are delimited by regions enriched with H3K4me3 (Figure 6K), suggesting that H3K4me3 might resist spreading of H3K9me3 and anchoring to the lamina. Remarkably, LAD boundaries are repositioned precisely at those sites demarcated by boundaries of H3K4me3 and H3K9me3, whereby H3K9me3 is enriched inside LADs and H3K4me3 just outside (Figure 6L). We addressed directly whether H3K4me3 can resist lamina anchoring by profiling H3K4me3 in embryos where LADs expand, namely in pool I (Figures 6M and S6K). These de novo broad LADs are also delimited by H3K4me3 domains (Figure 6N), which are largely unchanged (Figures 6M and S6M). We did not observe global changes in opposing modifications to those targeted by our pathways (Figures 6G, 6H, 6M, S3A, and S6M).

In summary, de novo LAD boundaries can form at places where H3K4me3 is delimited by H3K9me3. Our data suggest that anchoring of broad, ectopic H3K9me3 domains to the lamina is promoted by HP1 proteins and that H3K4me3 might resist spreading of H3K9me3 domains, preventing anchoring at the lamina. We conclude that embryos can reshuffle LADs based on the positional information of H3K9me3 and H3K4me3 domains (Figure 6O).

Developmental consequences associated with LAD disruption

Finally, we addressed the potential developmental relevance of LADs. Particularly, we investigated whether inheritance versus establishment of chromatin marks after fertilization makes different contributions to LAD establishment. We first focused on H3K27 methylation because of the known role of inherited maternal H3K27me3 in directing imprinting.[35] Combined expression of H3K27me3 demethylases Kdm6a(Utx) and Kdm6b (Jmjd3) strongly disrupted nuclear organization in zygotes (pool F) (Figure 1E) and affected genomic regions that are enriched in H3K27me3 in the oocyte but not in fertilized zygotes (Figure 2D). Thus, we next investigated whether zygotic LADs are regulated by maternal H3K27me3 and/or by de novo methylation of H3K27 after fertilization. We incubated embryos immediately after fertilization with GSK343,[36] an inhibitor of the H3K27 methyltransferase EZH2, and performed LaminB1-DamID in zygotes (Figure 7A). GSK343 treatment is expected to prevent the EZH2-dependent de novo methylation after fertilization, whereas Kdm6a/b expression should demethylate both de novo deposited and maternally inherited H3K27me3, the primary source of H3K27me3 in early zygotes.[37] Indeed, the extent of H3K27me3 reduction was more pronounced upon Kdm6a/b expression than EZH2 inhibition (Figure 7A).

Plotting DamID scores over control LAD boundaries indicated that EZH2 inhibition does not exert a major effect on zygotic LADs/iLADs (Figure 7B). DamID values in GSK343-treated embryos were similar to controls (Figure S7A). By contrast, zygotes

---

Figure 6. Manipulation of pathways rather than individual effectors interferes with LAD establishment and reorganization

(A and B) Enrichment of wild-type chromatin features in up genomic regions in zygotes and 2-cell embryos. Enrichment in control LADs and iLADs is shown for comparison. Positive compartment scores (Compart.) define A-compartment.

(C–F) Average Dam-LaminB1 OE value over control LAD boundaries comparing individual effectors (solid lines) to respective candidate pools (dotted lines).

(G and M) Dam-LaminB1 OE values and mean histone modification enrichment in 2-cell embryos over part of chromosome 6. Boxes indicate LADs. H3K9me3 domains established by HMM are shown as thick lines under the green tracks. Dotted rectangles in (G) depict examples of broad H3K9me3 domains corresponding to LADs in pool J.

(H) Representative single confocal planes from H3K9me3 immunostaining in late 2-cell-stage embryos. DAPI stains DNA. Asterisks, polar bodies; dashed lines mark cell membranes. Scale bars, 10 μm. N = 3.

(I and J) Metaplots showing average H3K9me3 enrichment or Dam-LaminB1 OE values over scaled wild-type B compartments in 2-cell embryos.

(K) Metaplot showing average H3K4me3 enrichment over scaled broad H3K9me3 domains in pool J.

(L) Average enrichment of histone modifications over de novo called 2-cell LAD boundaries in pool J.

(N) Average enrichment of H3K4me3 over de novo called LAD boundaries in 2-cell-stage embryos from pool I.

(O) Model depicting LAD boundary remodeling upon perturbation based on positional enrichment of H3K9me3 and H3K4me3 domains.

See also Figure S6 and Table S6.
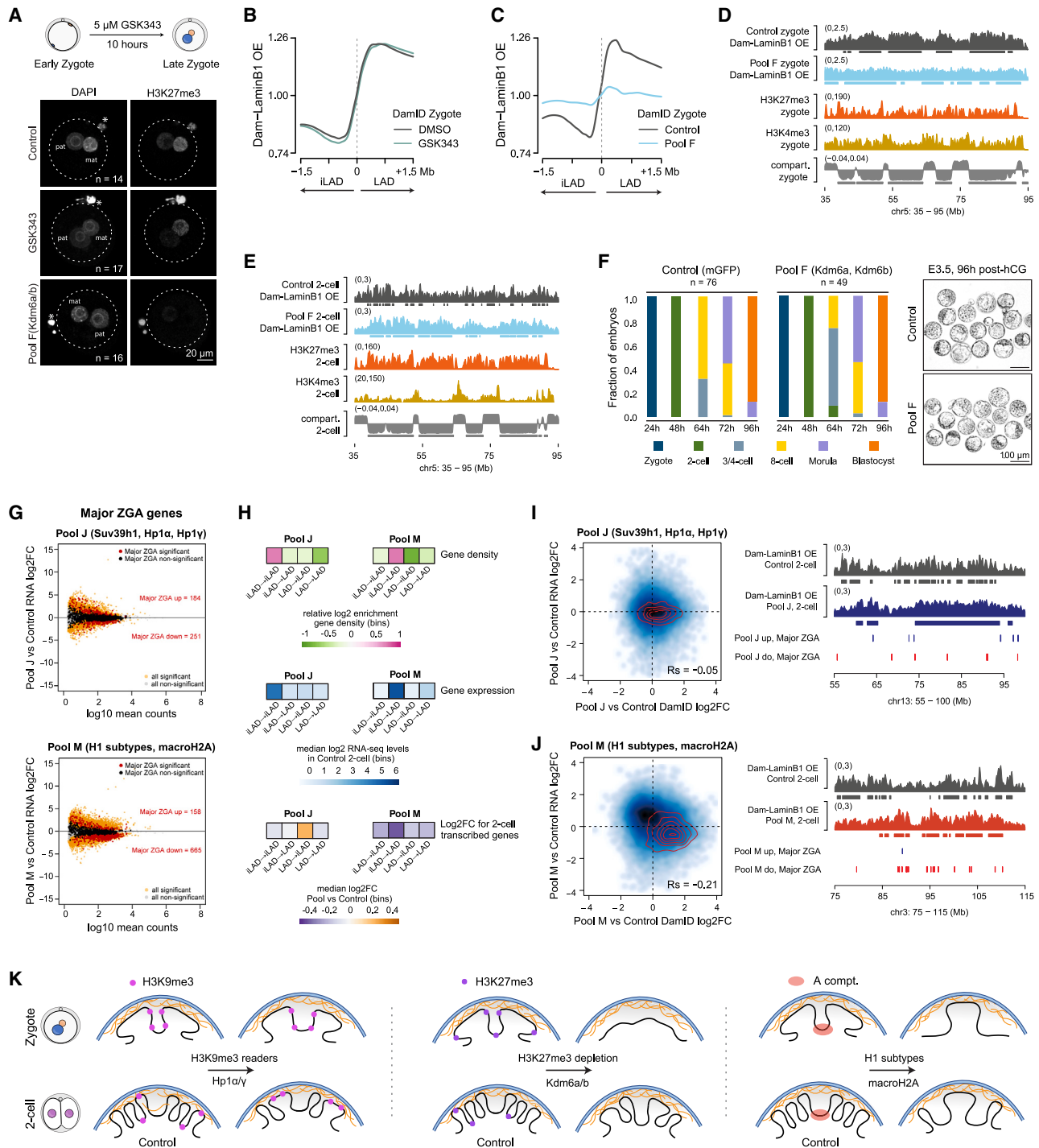
Figure 7. Developmental consequences associated with LAD disruption

(A) Maximum intensity projections of H3K27me3 immunostaining. H3K27me3 fluorescence signal is practically undetectable upon expression of Kdm6a/b. DAPI stains DNA. Asterisks, polar bodies; dashed lines, cell membranes; mat and pat, maternal and paternal pronucleus. Scale bar, 20 μm. N = 3.

(B and C) Average Dam-LaminB1 OE value over control zygotic LAD boundaries. Zero and dotted lines indicate LAD/iLAD boundary.

(D and E) Dam-LaminB1 OE value, histone modification enrichment, and compartment score from public datasets over part of chromosome5. Boxes represent LADs. Wild-type B compartments are indicated below compartment score tracks.

(F) Developmental progression and representative images at embryonic day 3.5 (E3.5) of embryos microinjected with mRNA for mGFP alone (control) or together with Kdm6a/b. h (x axis): hours post-hCG; n = total number of embryos analyzed from ≥3 independent experiments. Scale bars, 100 μm.

expressing Kdm6a/b exhibited striking changes (Figures 7C and S7B). Specifically, Kdm6a/b expression led to weaker contacts of LADs with the lamina that expanded beyond H3K27me3 regions into H3K4me3-enriched domains (Figure 7D). Continued expression of Kdm6a/b until the 2-cell stage had a milder effect (Figures 7E and S7C). These observations suggest that inherited H3K27me3 may be more important in setting up the LAD landscape in zygotes than at the 2-cell stage. This could be because maternal H3K27me3 levels demarcate zygotic LAD boundaries, but neither zygotic nor 2-cell H3K27me3 demarcate LAD boundaries of their corresponding stages (Figure S7D). Thus, inheritance rather than active H3K27 methylation contributes primarily to LAD formation in zygotes post-fertilization.

We analyzed the developmental competence of embryos expressing Kdm6a/b and found that they form blastocysts at comparable rates as controls (Figure 7F). We find this remarkable, as this posits that, despite major disruption of LADs in zygotes, embryos can rebuild nuclear architecture and continue successful preimplantation development. Next, we assessed developmental progression in representative perturbations that failed to restore LAD organization at the 2-cell stage. For all cases in which both zygotic and 2-cell LADs were disrupted, we observed a reduced rate of blastocyst formation (Figure S7E). These observations suggest that while zygotic LADs are dispensable for early development, 2-cell LADs are crucial.

Lastly, we explored the ways in which LAD disruption might be associated with gene expression changes during ZGA at the late 2-cell stage.[38–40] We focused on pathways exhibiting different LAD phenotypes: the constitutive heterochromatic pathway containing Suv39h1 and Hp1α/γ (pool J) and the H1 subtypes and macroH2A (pool M). Single-embryo RNA sequencing (RNA-seq) (Figure S7F) revealed gene expression changes in both perturbations with 3,311 and 6,551 upregulated and 2,558 and 5,042 downregulated genes in pools J and M, respectively (Table S7). Notably, upregulated genes include maternal transcripts (Figure S7G). While a developmental delay could contribute, PCA including several developmental stages suggests it is not the sole cause (Figure S7H). Differentially regulated genes also comprise major ZGA genes (Figure 7G). The stronger transcriptional defects in pool M correspond to gene-rich iLADs, which become repositioned toward the lamina (Figure 7H). LAD expansion into gene-poor, lowly expressed genomic regions in pool J elicits a comparatively weaker transcriptional phenotype (Figure 7H). Although regions that gain lamina interaction contain downregulated major ZGA genes, repositioning to and away from the lamina does not always entail changes in expression

(Figures 7I and 7J). This was particularly clear in pool N, where only 18 major ZGA genes are downregulated (Figure S7I; Table S7) despite major genome-lamina rearrangements (Figure 4B), and inversely, pool I displayed a milder genome-lamina rearrangement (Figure 4B) but more extensive transcriptional changes (442 major ZGA genes downregulated) (Figure S7J; Table S7). Thus, repositioning to and away from the lamina can be decoupled from changes in gene expression depending on the chromatin perturbation context. While it is likely that changes in gene expression result from multifactorial effects involving chromatin modifications and nuclear positioning, our data suggest that successful ZGA is associated with the correct genome-nuclear lamina organization in early embryos, yet ZGA can also be uncoupled from changes in nuclear organization.

DISCUSSION

Here, we generated a catalog of LAD disruption phenotypes (Figure S7K) and identified molecular players that disrupt nuclear architecture *in vivo*. We find zygotic LADs to be labile and highly sensitive to changes in heterochromatin-associated histone modifications. For example, while global depletion of H3K9me3 does not affect LAD establishment,[24] depositing or demethylating H3K9me2 through expressing the corresponding Kdm3a/b or Ehmt2 enzymes leads to a severe disruption of LADs. Thus, the specific balance of H3K9 di- and/or tri-methylation contributes to LAD architecture in zygotes.

Expression of Hp1α or Hp1γ does not affect zygotic LADs, but, consistently with the timing of heterochromatin maturation throughout the 2-cell stage, their expression leads to substantial remodeling of genome-lamina interactions at the 2-cell stage (Figure 7K, left). Overall, we identified four major pathways, primarily known to regulate heterochromatin, which perturb LAD establishment in zygotes and their reorganization at the 2-cell stage: (1) the constitutive H3K9me3 pathway, (2) a H3K4me2 and H3K9me2/K27me2 pathway regulated by demethylases Lsd1 and Kdm7a/c, (3) the H3K9me2/me3 writers Ehmt1/2 and Setdb1/2, and (4) the subtypes of H1 and macroH2A (Figure S7K).

Our data suggest a model whereby H3K4me3 delimits the spreading of H3K9me3 anchoring to the lamina, thereby determining the LAD boundaries (Figure 6O). Over-expression of the H3K9me3 reader/writer pathway overwrites the characteristic fragmented LADs, leading to a more canonical LAD structure in 2-cell-stage embryos. Thus, our observations also explain the unusual LAD fragmentation in wild-type 2-cell embryos, which

(G) MA plots of RNA-seq in 2-cell embryos. Differentially expressed (DE) genes, orange; non-differential, gray. DE major ZGA genes (DBTMEE classification), red; non-differential major ZGA genes, black.
(H) Enrichment for gene density (top), RNA-seq counts in control late 2-cell embryos (middle), and log$_2$ fold change (log2FC) in gene expression (bottom) for genes transcribed at the 2-cell stage (sum of DBTMEE categories: major ZGA, 2-cell transient, and MGA [mid-preimplantation gene activation] but excluding maternal RNA and minor ZGA) for genomic regions that reorganize between LAD and iLADs in pools J or M.
(I and J) Smoothed scatterplots of RNA-seq log2FC versus LaminB1 DamID log2FC between pools J or M and control late 2-cell embryos. Rs indicates Spearman's correlation. Red lines demarcate genomic bin density (n = 902) containing major ZGA genes but not maternal transcripts. Right: positions of upregulated (blue) or downregulated (red) major ZGA genes below the Dam-LaminB1 OE tracks.
(K) Summary of LAD reorganization upon perturbing H3K27, H3K9 methylation pathways, and histone content in zygote (top) and 2-cell embryos (bottom). Dots represent enrichment of histone modifications. Blue lines, nuclear envelope; orange mesh, nuclear lamina; red cloud, A compartments in control embryos.
See also Figure S7 and Table S7.

we propose is due to the non-canonical distribution of H3K4me3 and the lack of canonical H3K9me3 pathway at these stages. This also implies that H3K4me3 domains in early embryos contribute to maintaining robust nuclear organization and can counteract lamina anchoring. This builds on findings of KDM5B in LAD regulation in zygotes[24] and extends our understanding of the interplay between chromatin landscape and nuclear organization. Additionally, our data point toward a possible role for H3K27me2 in LAD organization in early embryos by potentially determining LAD boundary position, as expression of the H3K27me2 demethylase Kdm7a led to disrupted boundaries. On the other hand, H3K27me3 removal through Kdm6a/b resulted in expanded genome-lamina contacts inside the B compartment in 2-cell embryos. This is similar to human leukemia cells, where H3K27me3 may repel association to the lamina within B compartments.[41] Accordingly, recent findings in embryos lacking maternal EED, an essential component of the Polycomb Repressive Complex 2 (PRC2), indicate an antagonizing role for H3K27me3 in genome-lamina interactions, specifically with regards to LADs cell-to-cell variability at the 2-cell stage.[26] Thus, methylation of H3K27 plays a role in the robustness and definition of LAD boundaries in early embryos (Figure 7K, middle). Using a chemical inhibitor for EZH2 allowed disentangling the contribution of inherited versus *de novo* H3K27me3 and suggested that demethylation of inherited H3K27me3 contributes to a more drastic LAD phenotype. Indeed, we find H3K27me3 in oocytes enriched just outside future zygotic LAD boundaries, and active H3K27 demethylation rather than EZH2 inhibition leads to disrupted zygotic LADs. This is interesting, considering that oocytes lack detectable LADs, and suggests that maternal chromatin carries a "programming" mark for nuclear organization in embryos. Maternally inherited non-canonical H3K4me3 domains could serve a similar purpose by imparting a "stop" signal for H3K9me3 spreading during heterochromatin establishment.[42]

Chromatin decompaction is sufficient to relocate loci toward the nuclear interior.[16] Interactions that densify chromatin might guide preferential peripheral localization of condensed chromatin.[43] The association with the lamina of initially less dense A-compartment regions upon expression of histone deacetylases and histone H1 subtypes/macroH2A could reflect a favored repositioning due to increased compaction by histone deacetylation or by H1 subtypes and macroH2A[44–48] (Figure 7K, right). This agrees with the enrichment of the ectopically expressed histones in the nuclear periphery. These findings suggest that heterochromatic state influences nuclear organization in early embryos by promoting or impeding relocation of specific regions toward the periphery.

Our results suggest that the correct establishment of LADs in zygotes is dispensable for early development. Despite severe LAD disruption in zygotes by several candidates, genome-lamina interactions were successfully established after the first mitosis. This may suggest that nuclear organization in 2-cell embryos is more resilient compared with the apparently more labile nuclear-lamina contacts in zygotes inferred in this study. This may be because major ZGA occurs in 2-cell embryos, and transcriptional activity is highest just outside LAD boundaries at this stage.[25] Therefore, we speculate that ZGA might provide robustness to nuclear architecture in 2-cell embryos.

In summary, we show that a complex interplay of chromatin modifications influences the scaffolding of genome-lamina interactions post-fertilization and during MZT. Specific chromatin states are prone to altered lamina interactions under different perturbation conditions, and this behavior depends upon the developmental stage. Our work lays the ground for further investigation of embryonic chromatin and genome organization during early development.

Limitations of the study

Proteins produced in oocytes and inherited by zygotes and 2-cell embryos hinder the study of gene function at these stages. Genetic depletion is only achieved by conditional knockouts that must be performed in the germline, typically prior to oocyte growth. These strategies often lead to defects in germline development itself. The gain-of-function strategy of our screening enabled us to successfully interrogate multiple processes for a mid-scale screening coupled with low-input genomics *in vivo*. Although the use of DN constructs and demethylases targeting chromatin modifications allowed us to perform functional loss-of-function perturbations, further research is required to dissect the exact mechanistic processes leading to the LAD disruption phenotypes, as chromatin-modifying enzymes often target multiple histone marks and can have non-histone targets. Likewise, potential crosstalk between histone modifications cannot be ruled out, as it is known that modifications of specific residues depend on others, particularly those for which, e.g., methylation is processive. Our datasets could also be used for further exploration of the effects in the two parental genomes.

Cell
Resource

CellPress
OPEN ACCESS

AUTHOR CONTRIBUTIONS

M.P. performed study design, screening, experiments, and data analysis; T.S. performed data analysis; A.B., T.N., and F.P. contributed to experimental work; I.N., A.H.-G., and M.A.M.-R. contributed to data analysis; M.-E.T.-P. conceived, designed, and supervised the study.

DECLARATION OF INTERESTS

M.-E.T.-P. is a member of the Advisory Ethics Panel of Merck.

STAR★METHODS

Detailed methods are provided in the online version of this paper and include the following:

- KEY RESOURCES TABLE
- EXPERIMENTAL MODEL AND STUDY PARTICIPANT DETAILS
  - Embryo collection, culture, and manipulation
- METHOD DETAILS
  - DamID sample processing and library preparation
  - DamID sequencing and analysis
  - Allelic analysis of DamID dataset
  - RNA-seq library preparation and sequencing
  - RNA-seq analysis
  - CUT&RUN library generation and sequencing
  - CUT&Tag library generation and sequencing
  - Analysis of CUT&RUN and CUT&Tag data
  - Analysis of public chromatin datasets
  - Hi-C data analysis
  - Immunofluorescence
  - DNA FISH
  - DNA FISH image analysis
- QUANTIFICATION AND STATISTICAL ANALYSIS

SUPPLEMENTAL INFORMATION

Supplemental information can be found online at https://doi.org/10.1016/j.cell.2025.03.044.

REFERENCES

1. Gorkin, D.U., Leung, D., and Ren, B. (2014). The 3D Genome in Transcriptional Regulation and Pluripotency. Cell Stem Cell 14, 762–775. https://doi.org/10.1016/j.stem.2014.05.017.

2. Hauer, M.H., and Gasser, S.M. (2017). Chromatin and nucleosome dynamics in DNA damage and repair. Genes Dev. 31, 2204–2221. https://doi.org/10.1101/gad.307702.117.

3. Lieberman-Aiden, E., van Berkum, N.L., Williams, L., Imakaev, M., Ragoczy, T., Telling, A., Amit, I., Lajoie, B.R., Sabo, P.J., Dorschner, M.O., et al. (2009). Comprehensive mapping of long-range interactions reveals folding principles of the human genome. Science 326, 289–293. https://doi.org/10.1126/science.1181369.

4. Dixon, J.R., Selvaraj, S., Yue, F., Kim, A., Li, Y., Shen, Y., Hu, M., Liu, J.S., and Ren, B. (2012). Topological domains in mammalian genomes identified by analysis of chromatin interactions. Nature 485, 376–380. https://doi.org/10.1038/nature11082.

5. Sexton, T., Yaffe, E., Kenigsberg, E., Bantignies, F., Leblanc, B., Hoichman, M., Parrinello, H., Tanay, A., and Cavalli, G. (2012). Three-Dimensional Folding and Functional Organization Principles of the Drosophila Genome. Cell 148, 458–472. https://doi.org/10.1016/j.cell.2012.01.010.

6. Nora, E.P., Lajoie, B.R., Schulz, E.G., Giorgetti, L., Okamoto, I., Servant, N., Piolot, T., van Berkum, N.L., Meisig, J., Sedat, J., et al. (2012). Spatial partitioning of the regulatory landscape of the X-inactivation centre. Nature 485, 381–385. https://doi.org/10.1038/nature11049.

7. Ryba, T., Hiratani, I., Lu, J., Itoh, M., Kulik, M., Zhang, J., Schulz, T.C., Robins, A.J., Dalton, S., and Gilbert, D.M. (2010). Evolutionarily conserved replication timing profiles predict long-range chromatin interactions and distinguish closely related cell types. Genome Res. 20, 761–770. https://doi.org/10.1101/gr.099655.109.

8. Pope, B.D., Ryba, T., Dileep, V., Yue, F., Wu, W., Denas, O., Vera, D.L., Wang, Y., Hansen, R.S., Canfield, T.K., et al. (2014). Topologically associating domains are stable units of replication-timing regulation. Nature 515, 402–405. https://doi.org/10.1038/nature13986.

9. Pickersgill, H., Kalverda, B., de Wit, E., Talhout, W., Fornerod, M., and van Steensel, B. (2006). Characterization of the Drosophila melanogaster genome at the nuclear lamina. Nat. Genet. 38, 1005–1014. https://doi.org/10.1038/ng1852.

10. Guelen, L., Pagie, L., Brasset, E., Meuleman, W., Faza, M.B., Talhout, W., Eussen, B.H., de Klein, A., Wessels, L., de Laat, W., et al. (2008). Domain organization of human chromosomes revealed by mapping of nuclear lamina interactions. Nature 453, 948–951. https://doi.org/10.1038/nature06947.

11. van Steensel, B., and Belmont, A.S. (2017). Lamina-Associated Domains: Links with Chromosome Architecture, Heterochromatin, and Gene Repression. Cell 169, 780–791. https://doi.org/10.1016/j.cell.2017.04.022.

12. Briand, N., and Collas, P. (2020). Lamina-associated domains: peripheral matters and internal affairs. Genome Biol. 21, 85. https://doi.org/10.1186/s13059-020-02003-5.

13. Meuleman, W., Peric-Hupkes, D., Kind, J., Beaudry, J.-B., Pagie, L., Kellis, M., Reinders, M., Wessels, L., and van Steensel, B. (2013). Constitutive nuclear lamina–genome interactions are highly conserved and associated with A/T-rich sequence. Genome Res. 23, 270–280. https://doi.org/10.1101/gr.141028.112.

14. Peric-Hupkes, D., Meuleman, W., Pagie, L., Bruggeman, S.W.M., Solovei, I., Brugman, W., Gräf, S., Flicek, P., Kerkhoven, R.M., van Lohuizen, M., et al. (2010). Molecular maps of the reorganization of genome-nuclear lamina interactions during differentiation. Mol. Cell 38, 603–613. https://doi.org/10.1016/j.molcel.2010.03.016.

15. Tumbar, T., and Belmont, A.S. (2001). Interphase movements of a DNA chromosome region modulated by VP16 transcriptional activator. Nat. Cell Biol. 3, 134–139. https://doi.org/10.1038/35055033.

16. Therizols, P., Illingworth, R.S., Courilleau, C., Boyle, S., Wood, A.J., and Bickmore, W.A. (2014). Chromatin decondensation is sufficient to alter nuclear organization in embryonic stem cells. Science 346, 1238–1242. https://doi.org/10.1126/science.1259587.

17. Brueckner, L., Zhao, P.A., van Schaik, T., Leemans, C., Sima, J., Peric-Hupkes, D., Gilbert, D.M., and van Steensel, B. (2020). Local rewiring of genome-nuclear lamina interactions by transcription. EMBO J. 39, e103159. https://doi.org/10.15252/embj.2019103159.

18. Harr, J.C., Luperchio, T.R., Wong, X., Cohen, E., Wheelan, S.J., and Reddy, K.L. (2015). Directed targeting of chromatin to the nuclear lamina is mediated by chromatin state and A-type lamins. J. Cell Biol. 208, 33–52. https://doi.org/10.1083/jcb.201405110.

19. Yokochi, T., Poduch, K., Ryba, T., Lu, J., Hiratani, I., Tachibana, M., Shinkai, Y., and Gilbert, D.M. (2009). G9a selectively represses a class of late-replicating genes at the nuclear periphery. Proc. Natl. Acad. Sci. USA 106, 19363–19368. https://doi.org/10.1073/pnas.0906142106.

20. Wen, B., Wu, H., Shinkai, Y., Irizarry, R.A., and Feinberg, A.P. (2009). Large histone H3 lysine 9 dimethylated chromatin blocks distinguish differentiated from embryonic stem cells. Nat. Genet. 41, 246–250. https://doi.org/10.1038/ng.297.

21. Kind, J., Pagie, L., Ortabozkoyun, H., Boyle, S., de Vries, S.S., Janssen, H., Amendola, M., Nolen, L.D., Bickmore, W.A., and van Steensel, B. (2013).

Single-Cell Dynamics of Genome-Nuclear Lamina Interactions. Cell *153*, 178–192. https://doi.org/10.1016/j.cell.2013.02.028.

22. Bian, Q., Khanna, N., Alvikas, J., and Belmont, A.S. (2013). β-Globin cis-elements determine differential nuclear targeting through epigenetic modifications. J. Cell Biol. *203*, 767–783. https://doi.org/10.1083/jcb.201305027.

23. Amendola, M., and van Steensel, B. (2015). Nuclear lamins are not required for lamina-associated domain organization in mouse embryonic stem cells. EMBO Rep. *16*, 610–617. https://doi.org/10.15252/embr.201439789.

24. Borsos, M., Perricone, S.M., Schauer, T., Pontabry, J., Luca, K.L., de Vries, S.S., Ruiz-Morales, E.R., Torres-Padilla, M.-E., and Kind, J. (2019). Genome–lamina interactions are established de novo in the early mouse embryo. Nature *569*, 729–733. https://doi.org/10.1038/s41586-019-1233-0.

25. Pal, M., Altamirano-Pacheco, L., Schauer, T., and Torres-Padilla, M.-E. (2023). Reorganization of lamina-associated domains in early mouse embryos is regulated by RNA polymerase II activity. Genes Dev. *37*, 901–912. https://doi.org/10.1101/gad.350799.123.

26. Guerreiro, I., Rang, F.J., Kawamura, Y.K., Kroon-Veenboer, C., Korving, J., Groenveld, F.C., van Beek, R.E., Lochs, S.J.A., Boele, E., Peters, A.H.M.F., et al. (2024). Antagonism between H3K27me3 and genome–lamina association drives atypical spatial genome organization in the totipotent embryo. Nat. Genet. *56*, 2228–2237. https://doi.org/10.1038/s41588-024-01902-8.

27. Kind, J., Pagie, L., de Vries, S.S., Nahidiazar, L., Dey, S.S., Bienko, M., Zhan, Y., Lajoie, B., de Graaf, C.A., Amendola, M., et al. (2015). Genome-wide maps of nuclear lamina interactions in single human cells. Cell *163*, 134–147. https://doi.org/10.1016/j.cell.2015.08.040.

28. Pal, M., Kind, J., and Torres-Padilla, M.-E. (2021). DamID to Map Genome-Protein Interactions in Preimplantation Mouse Embryos. In Epigenetic Reprogramming During Mouse Embryogenesis: Methods and Protocols Methods in Molecular Biology, K. Ancelin and M. Borensztein, eds. (Springer), pp. 265–282. https://doi.org/10.1007/978-1-0716-0958-3_18.

29. Chaigne, A., Campillo, C., Voituriez, R., Gov, N.S., Sykes, C., Verlhac, M.-H., and Terret, M.-E. (2016). F-actin mechanics control spindle centring in the mouse zygote. Nat. Commun. *7*, 10253. https://doi.org/10.1038/ncomms10253.

30. Baarlink, C., Plessner, M., Sherrard, A., Morita, K., Misu, S., Virant, D., Kleinschnitz, E.-M., Harniman, R., Alibhai, D., Baumeister, S., et al. (2017). A transient pool of nuclear F-actin at mitotic exit controls chromatin organization. Nat. Cell Biol. *19*, 1389–1399. https://doi.org/10.1038/ncb3641.

31. Liang, Y., Franks, T.M., Marchetto, M.C., Gage, F.H., and Hetzer, M.W. (2013). Dynamic Association of NUP98 with the Human Genome. PLoS Genet. *9*, e1003308. https://doi.org/10.1371/journal.pgen.1003308.

32. Okuno, T., Li, W.Y., Hatano, Y., Takasu, A., Sakamoto, Y., Yamamoto, M., Ikeda, Z., Shindo, T., Plessner, M., Morita, K., et al. (2020). Zygotic Nuclear F-Actin Safeguards Embryonic Development. Cell Rep. *31*, 107824. https://doi.org/10.1016/j.celrep.2020.107824.

33. Wang, C., Liu, X., Gao, Y., Yang, L., Li, C., Liu, W., Chen, C., Kou, X., Zhao, Y., Chen, J., et al. (2018). Reprogramming of H3K9me3-dependent heterochromatin during mammalian embryo development. Nat. Cell Biol. *20*, 620–631. https://doi.org/10.1038/s41556-018-0093-4.

34. Burton, A., Brochard, V., Galan, C., Ruiz-Morales, E.R., Rovira, Q., Rodriguez-Terrones, D., Kruse, K., Le Gras, S., Udayakumar, V.S., Chin, H.G., et al. (2020). Heterochromatin establishment during early mammalian development is regulated by pericentromeric RNA and characterized by non-repressive H3K9me3. Nat. Cell Biol. *22*, 767–778. https://doi.org/10.1038/s41556-020-0536-6.

35. Inoue, A., Jiang, L., Lu, F., Suzuki, T., and Zhang, Y. (2017). Maternal H3K27me3 controls DNA methylation-independent imprinting. Nature *547*, 419–424. https://doi.org/10.1038/nature23262.

36. Verma, S.K., Tian, X., LaFrance, L.V., Duquenne, C., Suarez, D.P., Newlander, K.A., Romeril, S.P., Burgess, J.L., Grant, S.W., Brackley, J.A., et al. (2012). Identification of Potent, Selective, Cell-Active Inhibitors of the Histone Lysine Methyltransferase EZH2. ACS Med. Chem. Lett. *3*, 1091–1096. https://doi.org/10.1021/ml3003346.

37. Zheng, H., Huang, B., Zhang, B., Xiang, Y., Du, Z., Xu, Q., Li, Y., Wang, Q., Ma, J., Peng, X., et al. (2016). Resetting Epigenetic Memory by Reprogramming of Histone Modifications in Mammals. Mol. Cell *63*, 1066–1079. https://doi.org/10.1016/j.molcel.2016.08.032.

38. Zeng, F., and Schultz, R.M. (2005). RNA transcript profiling during zygotic gene activation in the preimplantation mouse embryo. Dev. Biol. *283*, 40–57. https://doi.org/10.1016/j.ydbio.2005.03.038.

39. Abe, K.I., Funaya, S., Tsukioka, D., Kawamura, M., Suzuki, Y., Suzuki, M.G., Schultz, R.M., and Aoki, F. (2018). Minor zygotic gene activation is essential for mouse preimplantation development. Proc. Natl. Acad. Sci. USA *115*, E6780–E6788. https://doi.org/10.1073/pnas.1804309115.

40. Schulz, K.N., and Harrison, M.M. (2019). Mechanisms regulating zygotic genome activation. Nat. Rev. Genet. *20*, 221–234. https://doi.org/10.1038/s41576-018-0087-x.

41. Siegenfeld, A.P., Roseman, S.A., Roh, H., Lue, N.Z., Wagen, C.C., Zhou, E., Johnstone, S.E., Aryee, M.J., and Liau, B.B. (2022). Polycomb-lamina antagonism partitions heterochromatin at the nuclear periphery. Nat. Commun. *13*, 4199. https://doi.org/10.1038/s41467-022-31857-5.

42. Sankar, A., Lerdrup, M., Manaf, A., Johansen, J.V., Gonzalez, J.M., Borup, R., Blanshard, R., Klungland, A., Hansen, K., Andersen, C.Y., et al. (2020). KDM4A regulates the maternal-to-zygotic transition by protecting broad H3K4me3 domains from H3K9me3 invasion in oocytes. Nat. Cell Biol. *22*, 380–388. https://doi.org/10.1038/s41556-020-0494-z.

43. MacPherson, Q., Beltran, B., and Spakowitz, A.J. (2020). Chromatin Compaction Leads to a Preference for Peripheral Heterochromatin. Biophys. J. *118*, 1479–1488. https://doi.org/10.1016/j.bpj.2020.01.034.

44. Gunjan, A., Alexander, B.T., Sittman, D.B., and Brown, D.T. (1999). Effects of H1 Histone Variant Overexpression on Chromatin Structure. J. Biol. Chem. *274*, 37950–37956. https://doi.org/10.1074/jbc.274.53.37950.

45. Thrower, D.A., and Bloom, K. (2001). Dicentric chromosome stretching during anaphase reveals roles of Sir2/Ku in chromatin compaction in budding yeast. Mol. Biol. Cell *12*, 2800–2812. https://doi.org/10.1091/mbc.12.9.2800.

46. Prendergast, L., and Reinberg, D. (2021). The missing linker: emerging trends for H1 variant-specific functions. Genes Dev. *35*, 40–58. https://doi.org/10.1101/gad.344531.120.

47. Chakravarthy, S., Patel, A., and Bowman, G.D. (2012). The basic linker of macroH2A stabilizes DNA at the entry/exit site of the nucleosome. Nucleic Acids Res. *40*, 8285–8295. https://doi.org/10.1093/nar/gks645.

48. Douet, J., Corujo, D., Malinverni, R., Renauld, J., Sansoni, V., Posavec Marjanović, M., Cantariño, N., Valero, V., Mongelard, F., Bouvet, P., et al. (2017). MacroH2A histone variants maintain nuclear organization and heterochromatin architecture. J. Cell Sci. *130*, 1570–1582. https://doi.org/10.1242/jcs.199216.

49. Ramsköld, D., Luo, S., Wang, Y.-C., Li, R., Deng, Q., Faridani, O.R., Daniels, G.A., Khrebtukova, I., Loring, J.F., Laurent, L.C., et al. (2012). Full-length mRNA-Seq from single-cell levels of RNA and individual circulating tumor cells. Nat. Biotechnol. *30*, 777–782. https://doi.org/10.1038/nbt.2282.

50. Deng, Q., Ramsköld, D., Reinius, B., and Sandberg, R. (2014). Single-Cell RNA-Seq Reveals Dynamic, Random Monoallelic Gene Expression in Mammalian Cells. Science *343*, 193–196. https://doi.org/10.1126/science.1245316.

51. Wu, J., Huang, B., Chen, H., Yin, Q., Liu, Y., Xiang, Y., Zhang, B., Liu, B., Wang, Q., Xia, W., et al. (2016). The landscape of accessible chromatin in mammalian preimplantation embryos. Nature *534*, 652–657. https://doi.org/10.1038/nature18606.

Cell
Resource

CellPress
OPEN ACCESS

52. Zhang, B., Zheng, H., Huang, B., Li, W., Xiang, Y., Peng, X., Ming, J., Wu, X., Zhang, Y., Xu, Q., et al. (2016). Allelic reprogramming of the histone modification H3K4me3 in early mammalian development. Nature *537*, 553–557. https://doi.org/10.1038/nature19361.

53. Xu, Q., Xiang, Y., Wang, Q., Wang, L., Brind'Amour, J., Bogutz, A.B., Zhang, Y., Zhang, B., Yu, G., Xia, W., et al. (2019). SETD2 regulates the maternal epigenome, genomic imprinting and embryonic development. Nat. Genet. *51*, 844–856. https://doi.org/10.1038/s41588-019-0398-7.

54. Dahl, J.A., Jung, I., Aanes, H., Greggains, G.D., Manaf, A., Lerdrup, M., Li, G., Kuan, S., Li, B., Lee, A.Y., et al. (2016). Broad histone H3K4me3 domains in mouse oocytes modulate maternal-to-zygotic transition. Nature *537*, 548–552. https://doi.org/10.1038/nature19360.

55. Liu, B., Xu, Q., Wang, Q., Feng, S., Lai, F., Wang, P., Zheng, F., Xiang, Y., Wu, J., Nie, J., et al. (2020). The landscape of RNA Pol II binding reveals a stepwise transition during ZGA. Nature *587*, 139–144. https://doi.org/10.1038/s41586-020-2847-y.

56. Lu, F., Liu, Y., Inoue, A., Suzuki, T., Zhao, K., and Zhang, Y. (2016). Establishing Chromatin Regulatory Landscape during Mouse Preimplantation Development. Cell *165*, 1375–1388. https://doi.org/10.1016/j.cell.2016.05.050.

57. Du, Z., Zheng, H., Huang, B., Ma, R., Wu, J., Zhang, X., He, J., Xiang, Y., Wang, Q., Li, Y., et al. (2017). Allelic reprogramming of 3D chromatin architecture during early mammalian development. Nature *547*, 232–235. https://doi.org/10.1038/nature23263.

58. Oomen, M.E., Rodriguez-Terrones, D., Kurome, M., Zakhartchenko, V., Mottes, L., Simmet, K., Noll, C., Nakatani, T., Mourra-Diaz, C.M., Aksoy, I., et al. (2025). An atlas of transcription initiation reveals regulatory principles of gene and transposable element expression in early mammalian development. Cell *188*, 1156–1174.e20. https://doi.org/10.1016/j.cell.2024.12.013.

59. Haraguchi, T., Koujin, T., Segura-Totten, M., Lee, K.K., Matsuoka, Y., Yoneda, Y., Wilson, K.L., and Hiraoka, Y. (2001). BAF is required for emerin assembly into the reforming nuclear envelope. J. Cell Sci. *114*, 4575–4585. https://doi.org/10.1242/jcs.114.24.4575.

60. Yang, M., and Yuan, Z.M. (2015). A novel role of PRR14 in the regulation of skeletal myogenesis. Cell Death Dis. *6*, e1734. https://doi.org/10.1038/cddis.2015.103.

61. Lombardi, M.L., Jaalouk, D.E., Shanahan, C.M., Burke, B., Roux, K.J., and Lammerding, J. (2011). The Interaction between Nesprins and Sun Proteins at the Nuclear Envelope Is Critical for Force Transmission between the Nucleus and Cytoskeleton. J. Biol. Chem. *286*, 26743–26753. https://doi.org/10.1074/jbc.M111.233700.

62. Vomastek, T., Iwanicki, M.P., Burack, W.R., Tiwari, D., Kumar, D., Parsons, J.T., Weber, M.J., and Nandicoori, V.K. (2008). Extracellular signal-regulated kinase 2 (ERK2) phosphorylation sites and docking domain on the nuclear pore complex protein Tpr cooperatively regulate ERK2-Tpr interaction. Mol. Cell. Biol. *28*, 6954–6966. https://doi.org/10.1128/MCB.00925-08.

63. Ye, J., Zhao, J., Hoffmann-Rohrer, U., and Grummt, I. (2008). Nuclear myosin I acts in concert with polymeric actin to drive RNA polymerase I transcription. Genes Dev. *22*, 322–330. https://doi.org/10.1101/gad.455908.

64. Provance, D.W., Addison, E.J., Wood, P.R., Chen, D.Z., Silan, C.M., and Mercer, J.A. (2008). Myosin-Vb functions as a dynamic tether for peripheral endocytic compartments during transferrin trafficking. BMC Cell Biol. *9*, 44. https://doi.org/10.1186/1471-2121-9-44.

65. Posern, G., Sotiropoulos, A., and Treisman, R. (2002). Mutant Actins Demonstrate a Role for Unpolymerized Actin in Control of Transcription by Serum Response Factor. Mol. Biol. Cell *13*, 4167–4178. https://doi.org/10.1091/mbc.02-05-0068.

66. Eid, A., Rodriguez-Terrones, D., Burton, A., and Torres-Padilla, M.-E. (2016). SUV4-20 activity in the preimplantation mouse embryo controls timely replication. Genes Dev. *30*, 2513–2526. https://doi.org/10.1101/gad.288969.116.

67. Deota, S., Chattopadhyay, T., Ramachandran, D., Armstrong, E., Camacho, B., Maniyadath, B., Fulzele, A., Gonzalez-de-Peredo, A., Denu, J.M., and Kolthur-Seetharam, U. (2017). Identification of a Tissue-Restricted Isoform of SIRT1 Defines a Regulatory Domain that Encodes Specificity. Cell Rep. *18*, 3069–3077. https://doi.org/10.1016/j.celrep.2017.03.012.

68. Mölder, F., Jablonski, K.P., Letcher, B., Hall, M.B., Tomkins-Tinch, C.H., Sochat, V., Forster, J., Lee, S., Twardziok, S.O., Kanitz, A., et al. (2021). Sustainable data analysis with Snakemake. F1000Res *10*, 33. https://doi.org/10.12688/f1000research.29032.2.

69. Bolger, A.M., Lohse, M., and Usadel, B. (2014). Trimmomatic: a flexible trimmer for Illumina sequence data. Bioinformatics *30*, 2114–2120. https://doi.org/10.1093/bioinformatics/btu170.

70. Dobin, A., Davis, C.A., Schlesinger, F., Drenkow, J., Zaleski, C., Jha, S., Batut, P., Chaisson, M., and Gingeras, T.R. (2013). STAR: ultrafast universal RNA-seq aligner. Bioinformatics *29*, 15–21. https://doi.org/10.1093/bioinformatics/bts635.

71. Jin, Y., Tam, O.H., Paniagua, E., and Hammell, M. (2015). TEtranscripts: a package for including transposable elements in differential expression analysis of RNA-seq datasets. Bioinformatics *31*, 3593–3599. https://doi.org/10.1093/bioinformatics/btv422.

72. Love, M.I., Huber, W., and Anders, S. (2014). Moderated estimation of fold change and dispersion for RNA-seq data with DESeq2. Genome Biol. *15*, 550. https://doi.org/10.1186/s13059-014-0550-8.

73. Langmead, B., and Salzberg, S.L. (2012). Fast gapped-read alignment with Bowtie 2. Nat. Methods *9*, 357–359. https://doi.org/10.1038/nmeth.1923.

74. Danecek, P., Bonfield, J.K., Liddle, J., Marshall, J., Ohan, V., Pollard, M.O., Whitwham, A., Keane, T., McCarthy, S.A., Davies, R.M., et al. (2021). Twelve years of SAMtools and BCFtools. GigaScience *10*, giab008. https://doi.org/10.1093/gigascience/giab008.

75. Quinlan, A.R., and Hall, I.M. (2010). BEDTools: a flexible suite of utilities for comparing genomic features. Bioinformatics *26*, 841–842. https://doi.org/10.1093/bioinformatics/btq033.

76. Filion, G.J., van Bemmel, J.G., Braunschweig, U., Talhout, W., Kind, J., Ward, L.D., Brugman, W., de Castro, I.J., Kerkhoven, R.M., Bussemaker, H.J., et al. (2010). Systematic Protein Location Mapping Reveals Five Principal Chromatin Types in Drosophila Cells. Cell *143*, 212–224. https://doi.org/10.1016/j.cell.2010.09.009.

77. Krueger, F., and Andrews, S.R. (2016). SNPsplit: Allele-specific splitting of alignments between genomes with known SNP genotypes. F1000Res *5*, 1479. https://doi.org/10.12688/f1000research.9037.2.

78. Martin, M. (2011). Cutadapt removes adapter sequences from high-throughput sequencing reads. EMBnet.journal *17*, 10–12. https://doi.org/10.14806/ej.17.1.200.

79. Huber, W., Carey, V.J., Gentleman, R., Anders, S., Carlson, M., Carvalho, B.S., Bravo, H.C., Davis, S., Gatto, L., Girke, T., et al. (2015). Orchestrating high-throughput genomic analysis with Bioconductor. Nat. Methods *12*, 115–121. https://doi.org/10.1038/nmeth.3252.

80. Schindelin, J., Arganda-Carreras, I., Frise, E., Kaynig, V., Longair, M., Pietzsch, T., Preibisch, S., Rueden, C., Saalfeld, S., Schmid, B., et al. (2012). Fiji: an open-source platform for biological-image analysis. Nat. Methods *9*, 676–682. https://doi.org/10.1038/nmeth.2019.

81. Berg, S., Kutra, D., Kroeger, T., Straehle, C.N., Kausler, B.X., Haubold, C., Schiegg, M., Ales, J., Beier, T., Rudy, M., et al. (2019). ilastik: interactive machine learning for (bio)image analysis. Nat. Methods *16*, 1226–1232. https://doi.org/10.1038/s41592-019-0582-9.

82. Park, S.-J., Shirahige, K., Ohsugi, M., and Nakai, K. (2015). DBTMEE: a database of transcriptome in mouse early embryos. Nucleic Acids Res. *43*, D771–D776. https://doi.org/10.1093/nar/gku1001.

83. Torres-Padilla, M.-E., Parfitt, D.-E., Kouzarides, T., and Zernicka-Goetz, M. (2007). Histone arginine methylation regulates pluripotency in the early

CellPress
OPEN ACCESS

Cell
Resource

mouse embryo. Nature *445*, 214–218. https://doi.org/10.1038/nature05458.

84. Burton, A., Muller, J., Tu, S., Padilla-Longoria, P., Guccione, E., and Torres-Padilla, M.-E. (2013). Single-cell profiling of epigenetic modifiers identifies PRDM14 as an inducer of cell fate in the mammalian embryo. Cell Rep. *5*, 687–701. https://doi.org/10.1016/j.celrep.2013.09.044.

85. Nakatani, T., Schauer, T., Altamirano-Pacheco, L., Klein, K.N., Ettinger, A., Pal, M., Gilbert, D.M., and Torres-Padilla, M.-E. (2024). Emergence of replication timing during early mammalian development. Nature *625*, 401–409. https://doi.org/10.1038/s41586-023-06872-1.

86. Skene, P.J., Henikoff, J.G., and Henikoff, S. (2018). Targeted in situ genome-wide profiling with high efficiency for low cell numbers. Nat. Protoc. *13*, 1006–1019. https://doi.org/10.1038/nprot.2018.015.

87. Hainer, S.J., and Fazzio, T.G. (2019). High-Resolution Chromatin Profiling Using CUT&RUN. Curr. Protoc. Mol. Biol. *126*, e85. https://doi.org/10.1002/cpmb.85.

88. Kaya-Okur, H.S., Janssens, D.H., Henikoff, J.G., Ahmad, K., and Henikoff, S. (2020). Efficient low-cost chromatin profiling with CUT&Tag. Nat. Protoc. *15*, 3264–3283. https://doi.org/10.1038/s41596-020-0373-x.

89. Miyanari, Y., Ziegler-Birling, C., and Torres-Padilla, M.-E. (2013). Live visualization of chromatin dynamics with fluorescent TALEs. Nat. Struct. Mol. Biol. *20*, 1321–1324. https://doi.org/10.1038/nsmb.2680.

STAR★METHODS

KEY RESOURCES TABLE

REAGENT or RESOURCE	SOURCE	IDENTIFIER
Antibodies		
Rabbit anti-H3K9me3	Abcam	Cat#ab8898; RRID:AB_306848
Rabbit anti-H3K9me3	Millipore	Cat#17-625; RRID:AB_916348
Mouse anti-H3K9me3	Active Motif	Cat#39286; RRID:AB_2935892
Rabbit anti-H3K4me3	EpiCypher	Cat#13-0041; RRID:AB_3076423
Rabbit anti-H3K4me3	Abcam	Cat#ab8580; RRID:AB_306649
Rabbit anti-H3K4me3	Diagenode	Cat#C15410003; RRID:AB_2924768
Rabbit anti-H3K27me3	Millipore	Cat#07-449; RRID:AB_310624
Rabbit anti-H3K27me2	Abcam	Cat#ab24684; RRID:AB_448222
Rabbit anti-H4K20me3	Millipore	Cat#07-463; RRID:AB_310636
Mouse anti-H3K9me2	Abcam	Cat#ab1220; RRID:AB_449854
Rabbit anti-H3K9me2	Active Motif	Cat#39239; RRID:AB_2793199
Rabbit anti-H3K9ac	Abcam	Cat#ab4441; RRID:AB_2118292
Goat anti-LaminB1	Santa Cruz	Cat#sc-6216; RRID:AB_648156
Rat anti-HA	Roche	Cat#11867423001; RRID:AB_390918
Guinea pig anti-Rabbit IgG secondary antibody	AntibodiesOnline	Cat#ABIN101961; RRID:AB_10775589
Goat anti-Rabbit IgG secondary antibody, Alexa 647	Invitrogen	Cat#A-21244; RRID:AB_2535812
Goat anti-Mouse IgG secondary antibody, Alexa 555	Invitrogen	Cat#A-21422; RRID:AB_2535844
Donkey anti-Goat IgG secondary antibody, Alexa 488	Invitrogen	Cat#A-11055; RRID:AB_2534102
Goat anti-Rat IgG secondary antibody, Alexa 594	Invitrogen	Cat#A-11007; RRID:AB_10561522
Biological samples		
Mouse preimplantation embryos	Torres-Padilla Lab	N/A
Chemicals, peptides, and recombinant proteins		
Pregnant mare serum gonadotropin (PMSG)	Ceva	Pregmagon®
Human chorionic gonadotrophin (hCG)	MSD Animal Health	Ovogest®
Hyaluronidase	Sigma Aldrich	Cat#H3506
KSOM	Torres-Padilla Lab	N/A
Paraffin oil	Sigma Aldrich	Cat#18512
Mineral oil	Sigma Aldrich	Cat#8410
3-Indoleacetic acid (Auxin)	Sigma Aldrich	Cat#I2886
Dimethyl sulfoxide (DMSO)	Invitrogen	Cat#D12345
GSK343	Selleckchem	Cat#S7164
Pronase	Roche	Cat#10165921001
M2 Medium	Sigma Aldrich	Cat#M7167
Trypsin-EDTA (0.25%)	Thermo Fisher	Cat#25200056
10x PBS buffer, pH 7.4	Thermo Fisher	Cat#AM9624
10x lysis buffer	Clontech	Cat#635013
dNTP mix	Thermo Fisher	Cat#R0192
RNase inhibitor	Takara	Cat#2313A

Continued

REAGENT or RESOURCE	SOURCE	IDENTIFIER
Superscript II RT	Thermo Fisher	Cat#18064014
Betaine	Sigma Aldrich	Cat#B0300-1VL
PEG-8000	Sigma Aldrich	Cat#P1458
HiFi ReadyMix	KAPA	Cat#KM2605
1,4-Dithiothreitol (DTT)	Sigma Aldrich	Cat#D9779
$MgCl_2$	Sigma Aldrich	Cat#M1028
Spermidine	Sigma Aldrich	Cat#S2626
Protease inhibitor cocktail tablets	Roche	Cat#11873580001
NaCl (5M)	Invitrogen	Cat#AM9760G
Triton-X 100 solution (10%)	Sigma Aldrich	Cat#93443
0.5 M EDTA, pH 8.0	Invitrogen	Cat#15575-038
EGTA	Sigma Aldrich	Cat#3889
pAG-MNase	EpiCypher	Cat#15-1016
$CaCl_2$	Sigma Aldrich	Cat#C7902
Glycogen	Thermo Fisher	Cat#R0551
RNaseA	Thermo Fisher	Cat#EN0531
pA-Tn5 adaptor complex	Diagenode	Cat#C01070001
SDS solution (10%)	Promega	Cat#6551
NEBNext high-fidelity PCR master mix	NEB	Cat#M0541
Paraformaldehyde	Sigma Aldrich	Cat#P6148
Formaldehyde, methanol-free (16%)	Thermo Fisher	Cat#11586711
Bovine serum albumin (BSA)	Sigma Aldrich	Cat#A3311
Tween 20	Sigma Aldrich	Cat#P1379
Vectashield antifade mounting medium with DAPI	Vector Laboratories	Cat#H-2000
dATP	Thermo Fisher	Cat#R0141
dCTP	Thermo Fisher	Cat#R0151
dGTP	Thermo Fisher	Cat#R0161
Aminoallyl-dUTP-ATTO-550	Jena Bioscience	Cat#NU-803-550
Aminoallyl-dUTP-XX-ATTO-594	Jena Bioscience	Cat#NU-803-XX-594
Aminoallyl-dUTP-ATTO-647N	Jena Bioscience	Cat# NU-803-647N
Polyvinylpyrrolidone (PVP)	Sigma Aldrich	Cat#PVP40
Hydrochloric acid solution	Sigma Aldrich	Cat#H9892
Dextran sulphate sodium salt	Sigma Aldrich	Cat#D8906
Formamide	Sigma Aldrich	Cat#F9037
20x SSC buffer	Sigma Aldrich	Cat#S6639
Mouse Cot-1 DNA	Invitrogen	Cat#18440016
Klenow fragment (3' to 5' exo-)	NEB	Cat#M0212
T4 DNA ligase	NEB	Cat#M0202
2x MyTaq red mix	Bioline	Cat#BIO-25043
DpnI	NEB	Cat#R0176
NP-40 (10%)	Biovision	Cat#2111-100
Proteinase K	Invitrogen	Cat#2546
Critical commercial assays		
mMESSAGE mMACHINE T3 Transcription Kit	Invitrogen	Cat#AM1348
mMESSAGE mMACHINE T7 ULTRA Transcription Kit	Invitrogen	Cat#AM1345

(Continued on next page)

Cell
Resource

CellPress
OPEN ACCESS

Continued

REAGENT or RESOURCE	SOURCE	IDENTIFIER
End-It DNA end-repair kit	Epicentre	Cat#ER81050
QIAquick PCR purification kit	Qiagen	Cat#28104
AMPure RNA magnetic beads	Beckman Coulter	Cat#A63987
AMPure XP DNA magnetic beads	Beckman Coulter	Cat#A63881
Nextera XT	Illumina	Cat#15032354
NucleoBond BAC 100 kit	Macherey-Nagel	Cat#740579
Nick translation mix	Roche	Cat#10976776001
Deposited data		
Single-cell RNA-seq data of mouse oocytes and preimplantation embryos	Ramsköld et al.[49]; Deng et al.[50]	GEO: GSE38495, GSE45719
ATAC-seq	Wu et al.[51]	GEO: GSE66581
H3K4me3 ChIP data	Zhang et al.[52]	GEO: GSE71434
H3K36me3 ChIP data	Xu et al.[53]	GEO: GSE112834
H3K27ac ChIP data	Dahl et al.[54]	GEO: GSE72784
H3K9me3 ChIP data	Wang et al.[33]	GEO: GSE98149
H3K27me3 ChIP data	Zheng et al.[37]	GEO: GSE76687
Pol2 Stacc-seq data	Liu et al.[55]	GEO: GSE135457
DNaseI-seq data	Lu et al.[56]	GEO: GSE76642
Hi-C data	Du et al.[57]	GEO: GSE82185
Single-embryo RNA-seq (SMART-seq+5′)	Oomen et al.[58]	GEO: GSE225056
Embryo LaminB1 DamID data and Allelic LAD coordinates	Borsos et al.[24]	GEO: GSE112551
α-amanitin treatment LaminB1 DamID data	Pal et al.[25]	GEO: GSE241483
LaminB1 DamID	This paper	GEO: GSE244496
H3K9me3 CUT&RUN	This paper	GEO: GSE278718
H3K4me3 CUT&Tag	This paper	GEO: GSE278719
Single-embryo RNA-seq (SMART-seq+5′)	This paper	GEO: GSE278720
Experimental models: Organisms/strains		
Mouse: F1 (C57BL/6J × CBA/H) females	Janvier Labs	MGI:5650652
Mouse: DBA/2J males	Janvier Labs	MGI:2684695
Oligonucleotides		
DamID Adapter_top: 5'-CTAATACGACT CACTATAGGGCAGCGTGGTCG CGGCCGAGGA-3'	Sigma Aldrich	N/A
DamID Adapter_bottom: 5'-TCCTCGGCCGCG-3'	Sigma Aldrich	N/A
Barcoded DamID PCR primers: 5'-NNNNNNBAR CODGTGGTCGCGGCCGAGGATC-3'	Sigma Aldrich	N/A
ERCC RNA spike in mix	Invitrogen	Cat#4456740
oligo-dT30V: 5'-AAGCAGTGGTATCA ACGCAGAGTACT30V-3'	Sigma Aldrich	N/A
TSO:5'-AAGCAGTGGTATCAACG CAGAGTACATrGrG+G-3'	TIB MolBiol	N/A
ISPCR oligo: 5'-AAGCAGTGGTA TCAACGCAGAGT-3'	Biomers.net	N/A
Illumina sequencing adaptor mix and primers	IDT or Sigma Aldrich	N/A
Recombinant DNA		
pRN3P-AID-Dam-LaminB1	Borsos et al.[24]	N/A
pRN3P-TIR1-3XMyc	Borsos et al.[24]	Addgene #119766
pRN3P-EGFP-m6ATracer	Borsos et al.[24]	Addgene #139403

(Continued on next page)

Continued

REAGENT or RESOURCE	SOURCE	IDENTIFIER
pRN3P-membrane-EGFP	Borsos et al.[24]	Addgene #139402
pRN3P-GFP	Burton et al.[34]	N/A
pRN3P-HA-DN-Baf-G25E	Haraguchi et al.[59]	N/A
pRN3P-HA-DN-Prr14	Yang et al.[60]	N/A
pRN3P-HA-mCherry-DN Syne1	Lombardi et al.[61]	N/A
pRN3P-HA-Exportin6	Baarlink et al.[30]	N/A
pRN3P-EzrinTD-mCherry-VCA	Chaigne et al.[29]	N/A
pcDNA3-Flag-Tpr	Vomastek et al.[62]	Addgene #60882
pRN3P-HA-del-Nup98	Liang et al.[31]	N/A
pRN3P-HA-DN-NM1	Ye et al.[63]	N/A
pGEMHE-mCherry-MyoVbTail	Provance et al.[64]	N/A
pRN3P-HA-NLS-Actin-R62D	Posern et al.[65]	N/A
pRN3P-Hdac3-Flag	This paper	N/A
pRN3P-HA-Kdm6a	This paper	N/A
pcDNA-Flag-Kdm6b(1025-End)-pA	Inoue et al.[35]	Addgene #100278
pRN3P-HA-Set8	This paper	N/A
pRN3P-HA-Suv420h1	Eid et al.[66]	Addgene #86689
pRN3P-HA-Suv420h2	Eid et al.[66]	Addgene #86691
pRN3P-HA-Kdm3a	This paper	N/A
pRN3P-HA-Kdm3b	This paper	N/A
pRN3P-HA-Lsd1	This paper	N/A
pRN3P-HA-Kdm7a	This paper	N/A
pRN3P-HA-Kdm7c	This paper	N/A
pRN3P-HA-Suv39h1	Burton et al.[34]	N/A
pRN3P-HA-Hp1α	This paper	N/A
pRN3P-HA-Hp1γ	This paper	N/A
pRN3P-HA-Phf19	This paper	N/A
pRN3P-HA-G2e3	This paper	N/A
pRN3P-HA-Dhx33	This paper	N/A
pRN3P-Hdac1-HA	This paper	N/A
pRN3P-Hdac6-HA	This paper	N/A
pcDNA3-Flag-Sirt1	Deota et al.[67]	Addgene #105670
pRN3P-HA-H1.2	This paper	N/A
pRN3P-HA-H1.4	This paper	N/A
pRN3P-HA-H1.5	This paper	N/A
pRN3P-HA-macroH2A.1.1	This paper	N/A
pRN3P-HA-Ehmt1	This paper	N/A
pRN3P-HA-Ehmt2	Burton et al.[34]	N/A
pRN3P-HA-Setdb1	Burton et al.[34]	N/A
pRN3P-HA-Sedb2	Burton et al.[34]	N/A
BAC DNAs, see Table S1	BACPAC	N/A
Software and algorithms		
Snakemake	Mölder et al.[68]	https://snakemake.github.io
R	R Core Team	https://www.r-project.org
Trimmomatic	Bolger et al.[69]	http://www.usadellab.org/cms/?page=trimmomatic
STAR	Dobin et al.[70]	https://github.com/alexdobin/STAR
TEtranscripts (TEcount)	Jin et al.[71]	https://hammelllab.labsites.cshl.edu/software/
DEseq2	Love et al.[72]	https://bioconductor.org/packages/release/bioc/html/DESeq2.html

(Continued on next page)

Cell
Resource

Continued

REAGENT or RESOURCE	SOURCE	IDENTIFIER
FASTX barcode splitter	Hannon Lab	https://github.com/agordon/fastx_toolkit
Bowtie2	Langmead and Salzberg[73]	https://bowtie-bio.sourceforge.net/bowtie2/index.shtml
Samtools	Danecek et al.[74]	https://www.htslib.org/doc/samtools.html
Picard	Broad Institute	https://broadinstitute.github.io/picard/
BEDTools	Quinlan and Hall[75]	https://bedtools.readthedocs.io/en/latest/
Hidden Markov model (HMMt)	Filion et al.[76]	https://github.com/gui11aume/HMMt
SNPsplit	Krueger and Andrews[77]	https://www.bioinformatics.babraham.ac.uk/projects/SNPsplit/
Cutadapt	Martin[78]	https://cutadapt.readthedocs.io/en/stable/
Bioconductor	Huber et al.[79]	https://bioconductor.org
Fiji	Schindelin et al.[80]	https://imagej.net/software/fiji/
ilastik	Berg et al.[81]	https://www.ilastik.org/
Other		
Script for DNA FISH data analysis	This paper	https://ascgitlab.helmholtz-munich.de/public_microscopy/pal-et-al-image-analysis
TE annotations	Hammell Lab	https://labshare.cshl.edu/shares/mhammelllab/www-data/TEtranscripts/TE_GTF/mm10_rmsk_TE.gtf.gz
Mouse reference genome GRCm38	ENSEMBL	http://ftp.ensembl.org/pub/release-101/fasta/mus_musculus/dna/Mus_musculus.GRCm38.dna.primary_assembly.fa.gz
SNP annotation for GRCm38	EBI UK	https://ftp.ebi.ac.uk/pub/databases/mousegenomes/REL-1505-SNPs_Indels/mgp.v5.merged.snps_all.dbSNP142.vcf.gz
ERCC spike-in sequences and annotations	Thermo Fisher	https://assets.thermofisher.com/TFS-Assets/LSG/manuals/ERCC92.zip
Gene annotations (gencode)	ENSEMBL	http://ftp.ebi.ac.uk/pub/databases/gencode/Gencode_mouse/release_M20/gencode.vM20.primary_assembly.annotation.gtf.gz
DBTMEE gene classification	Park et al.[82]	https://dbtmee.hgc.jp/download/data/tables.tar.gz
BACs	BACPAC	https://bacpacresources.org/home.htm

EXPERIMENTAL MODEL AND STUDY PARTICIPANT DETAILS

Embryo collection, culture, and manipulation

All experiments were approved by the Government of Upper Bavaria. Mice housed in Helmholtz Zentrum München were maintained and bred in accordance with institutional guidelines. To obtain embryos, 5 to 8-week-old F1 (C57BL/6J × CBA/H) female mice were mated with DBA/2J males. To induce ovulation, females were injected with 10 IU pregnant mare serum gonadotropin (PMSG) (Ceva) and then 46-48 h later with human chorionic gonadotrophin (hCG) (MSD Animal Health). Collected embryos were cultured in KSOM drops under paraffin oil (Sigma) at 37 °C with 5% CO_2 as previously described. For DamID, early zygotes (18h post-hCG) were isolated and injected with 250 ng/μL Tir1, 50 ng/μL membrane-eGFP (mGFP) and 10 ng/μL AID-Dam-LaminB1 along with mRNA encoding candidate protein(s) and cultured in auxin (500 μM)-containing medium. For mapping LADs in the zygotic stage, auxin was removed from 22 h and late zygotes were collected at 28–30h post-hCG. For DamID in the late 2-cell stage, auxin was washed out from 42 to 48-50h post-hCG and embryos were cultured in KSOM. All dominant negative constructs[29–31,59–61,63,65] and candidate cDNAs were subcloned into the pRN3P vector containing identical 5' and 3'UTR and a consensus KOZAK to ensure efficient and equivalent expression (excepting for Kdm6b,[35] Tpr[62] and Sirt1,[67] which were already obtained in pcDNA, and MyoVbTail[64] in pGEMHE, both suitable for *in vitro* transcription). The mRNA concentration of candidate proteins was decided based on the size of the ORF and was chosen based on earlier titration experiments.[24,34,66,83–85] The concentration of mRNA used was calculated to ensure a molarity equivalence range (0.8-1.5 μM) across all candidates, both for the individually microinjected candidates or within the pools, to achieve a similar equimolar expression (Table S1). mRNAs were transcribed *in vitro* from linearized plasmid constructs using suitable mMESSAGE mMACHINE kits (Invitrogen). For the EZH2 inhibition experiment in zygote, embryos were treated with 0.01% DMSO (as control) or 5 μM GSK343 (Selleckchem, #S7164) from 18h to 28h post-hCG. To monitor developmental effects,

microinjected embryos were scored daily after microinjection, up until day 4. As control, we used embryos injected with mRNA for membrane-eGFP only. To validate for the expression of candidate Pools and individual proteins, we performed immunostaining against HA, the targeted histone modification, or monitored fluorescent of fusion proteins (e.g., mCherry-DN Syne1,[61] mCherry-cVCA[29] and mCherry-MyoVbTail[64]). For the Pools containing structural nuclear membrane components or exportin and actin dominant negative constructs (Pool B and Pool E), validation of expression was inferred from the expected published phenotype, namely lack of cell division[29] and reduced pronuclear size, respectively (Figure S1H).

METHOD DETAILS

DamID sample processing and library preparation

Zona pellucida was removed by treatment with 0.5% pronase in M2 at 37 °C for 5 minutes with visual inspection. Polar bodies were separated from the embryos by gentle pipetting after a short trypsin treatment (up to 1 minute with visual inspection) and discarded. For each replicate, a pool of 10-20 blastomeres (10 to 20 zygotes or 5 to 10 2-cell embryos) were collected in 2 μL DamID buffer (10 mM TRIS acetate pH 7.5, 10 mM magnesium acetate, 50 mM potassium acetate) and stored at -80 °C until processing. All experiments were performed in at least three independent biological replicates. Sample processing and library preparation were done as described.[24,28]

DamID sequencing and analysis

Samples were sequenced using Illumina HiSeq4000 or HiSeq2500 platforms in 150 bp PE mode but only read1 was used for analysis. For read pre-processing, the first 6 random bases were discarded using trimmomatic[69] (version 0.39). Subsequently, reads were de-multiplexed according to DamID indexes using fastx barcode splitter and the additional 15 bp of adaptors were trimmed using trimmomatic. Pre-processed reads starting with GATC were then mapped to the GRCm38 using bowtie2[73] (version 2.5.1) with default parameters. Reads aligning to the genome with a quality score below 30 were discarded using samtools[74] (version 1.17). Duplicates were removed using picard (version 3.0.0) to obtain unique GATC reads. Reads were counted in 100-kb consecutive genomic bins using bedtools[75] (version 2.31.0). The computation of OE (Observed/Expected) values per bin was carried out similarly as described.[27] Briefly, to obtain the expected number of reads, all genomic GATC sites were extended to the trimmed read length (123 bp) in both directions with R (version 4.1.2) using Bioconductor[79] packages Biostrings (version 2.62.0) and GenomicRanges (version 1.46.1). Extended GATC reads were processed the same way as reads obtained by DamID (observed). Read counts were normalized by rpkm (reads per kilobase per million) and a pseudo-count was added (smallest non-zero rpkm value). Finally, the observed over expected rpkm ratio was calculated. Bins with zero rpkm for both observed and expected values were treated as zero. For obtaining the OE mean signal, rpkm values of at least three replicates were averaged prior OE value calculation. The OE mean signal was used for data visualization and LAD calling. To distinguish LAD domains from inter-LADs, a two-state hidden Markov model (HMM)[76] was applied to non-zero OE mean values. All data processing was performed using a custom Snakemake[68] pipeline.

Allelic analysis of DamID dataset

Allelic analysis was performed using SNPsplit[77] (version 0.6.0). SNP annotation for GRCm38 genome was downloaded from https://ftp.ebi.ac.uk/pub/databases/mousegenomes/REL-1505-SNPs_Indels/mgp.v5.merged.snps_all.dbSNP142.vcf.gz. Genome files were prepared using SNPsplit_genome_preparation with the parameters –strain CBA_J –strain2 DBA_2J. SNPsplit was applied on the DamID alignment files using 1,708,377 DBA/2J-specific SNPs. To obtain allelic OE values, the splitting was also carried out on the genomic GATC reads, which served as allelic expected read counts. For downstream analysis, only those genomic bins were considered that contained more than 30 allele-specific genomic GATC reads and thus the allelic analysis is limited to 4,254 100-kb bins. Allelic OE values were visualized at LADs/iLADs using our previously published maternal and paternal LAD coordinates.[24]

RNA-seq library preparation and sequencing

The SMART-seq+5' protocol was adapted from the Smart-seq2 protocol as described.[58] For each batch, late 2-cell stage embryos (batch 1: membrane-eGFP control, Pool J, and Pool M; batch 2: membrane-eGFP control, Pool I, and Pool N) were collected in the same lysis buffer, stored at -80 °C until use. The lysis buffer was prepared by diluting Clontech 10× lysis buffer (#635015) to 1× in H2O, supplemented with ERCC RNA spike-ins (diluted to 1: 581,000), and aliquoted into PCR tubes (5.8 μL per tube). The embryos were washed three times in PBS, transferred to tubes containing the lysis buffer, snap-frozen in liquid nitrogen, and stored at -80 °C until further processing. RNA was extracted using AMPure RNA magnetic beads (Beckman Coulter), washed with 80% ethanol, and resuspended in 1 μL of dNTP mix (ThermoFisher, R0192), 1 μL of oligo-dT30V (10 μM, Sigma, 5'-AAGCAGTGGTATCAACGCAGAG TACT30V-3'), and 1 μL of nuclease-free water containing 5% RNase inhibitor (Takara, 2313A). The samples were incubated for 3 minutes at 72 °C and kept on ice until further processing. The reverse transcription solution was prepared by mixing 2 μL of Superscript II 5× RT buffer (Thermo-Fisher, 18064014), 1.6 μL of 40% PEG-8000 (Sigma), 0.5 μL of DTT, 0.25 μL of RNase inhibitors (Takara, 2313A), 0.1 μL of 100 μM TSO (TIB MolBiol, 5'-AAGCAGTGGTATCAACGCAGAGTACATrGrG+G-3'), 0.06 μL of 1M MgCl2 (Sigma, M1028), 2 μL of 5M Betaine (Sigma, B0300), and 0.5 μL of Superscript II RT. A total of 7 μL of this reverse transcription mix was added to the 3 μL of the annealed RNA mix, and the mixture was incubated for 90 minutes at 42 °C, followed by 15 minutes at 70 °C. Pre-amplification of the resulting cDNA was performed using KAPA HiFi ReadyMix (KM2605) for 14 cycles with ISPCR primers (10 μM,

Cell
Resource

Sigma, 5'-AAGCAGTGGTATCAACGCAGAGT-3') and the product was purified using Agencourt AMPure XP beads (Beckman Coulter). For each sample, 2.5 μL of 120 μg/μL cDNA was used for tagmentation, which was carried out using the Nextera XT kit (Illumina, 15032354). The preamplified cDNA was mixed with 5 μL of tagment DNA buffer and 2.5 μL of Amplicon Tagment Mix, and the reaction was incubated at 55 °C for 5 minutes. The tagmentation reaction was stopped with 2.5 μL of NT buffer, and the samples were incubated at room temperature for 5 minutes. The tagmented DNA was then amplified for 12 cycles using the standard i5 and i7 Nextera Unique Double Indexes along with a tailed i7 index, which contains an overhang enabling the capture of the 5' end of the transcripts. The libraries were sequenced in 150 bp paired-end mode using the Illumina NovaSeq6000 platform.

RNA-seq analysis

RNA-seq read pairs were aligned to the mouse reference (GRCm38 primary assembly genome) using STAR[70] (version 2.7.6a) and the gencode annotation (vM20). ERCC spike-in sequences and annotations were obtained from https://assets.thermofisher.com/TFS-Assets/LSG/manuals/ERCC92.zip. ERCC, human SUV39H1 and membrane-eGFP sequences were added to the reference genome prior to alignment. STAR parameters were set to –outFilterMultimapNmax 100 –winAnchorMultimapNmax 100. Reads were counted at genes and transposable elements (TE) using TEcount[71] with the parameters –mode multi –stranded no. TE annotation was obtained from https://labshare.cshl.edu/shares/mhammelllab/www-data/TEtranscripts/TE_GTF/mm10_rmsk_TE.gtf.gz. Only samples that met our quality criteria of at least 500 thousand read counts, less than 15 percent mitochondrial and ERCC reads, respectively, were included in the analysis. Genes and TEs with at least one read detected in one fourth of the samples were considered. Differential expression analysis was performed using DESeq2[72] (version 1.26.0) for each batch of embryos separately in R (version 3.6.3). Read counts were normalized by the default DESeq2 method. Results were visualized on MA-plots for which genes were colored by significance (adjusted p-value < 0.05) and labeled according to DBTMEE[82] gene clusters. DBTMEE data were obtained from the table cluster_gene.tsv at the link https://dbtmee.hgc.jp/download/data/tables.tar.gz. For principal component analysis (PCA), normalized counts were log_2 transformed after adding a pseudo-count of 1. For combined PCA, SMART-seq+5' data for different embryonic stages was obtained from GSE225056.[58] To generate RNA-seq genome coverages, STAR alignments were filtered for uniquely mapped reads by samtools (version 1.16.1) with the parameter -q 255. Read pairs were counted in 100-kb consecutive bins (same bin size as for DamID profiles), normalized by the sum of the counts, and multiplied by a million. Replicates were averaged for downstream analysis. The bin-based log_2 fold change between Pool vs. Control of the RNA-seq was directly compared to the log_2 fold change of the DamID data. To assess the expression levels of candidates in early embryos (Table S1), mean rpkms were calculated using single-embryo RNA-seq data available from GSE38495[49] and GSE45719.[50]

CUT&RUN library generation and sequencing

CUT&RUN (Cleavage Under Targets & Release Using Nuclease) for H3K9me3 was conducted following the published protocol[86] with modifications for embryos. 60 to 80 late 2-cell stage embryos (48h post-hCG) with intact zona pellucida were washed three times in a buffer containing 20 mM HEPES-NaOH pH 7.5, 150 mM NaCl, 0.5 mM spermidine, 0.1% BSA, and 1× Roche protease inhibitor cocktail. The embryos were then transferred to antibody buffer (1:100 dilution of anti-H3K9me3 antibody (Abcam, ab8898 or Millipore, 17–625) in wash buffer containing 0.05% Triton-X and 2 mM EDTA pH 8.0). After overnight incubation with the antibody at 4 °C, embryos were washed in Triton wash buffer (wash buffer containing 0.05% Triton-X) and incubated with pAG-MNase (1:20 or 1:200 dilution; EpiCypher, 15–1016) for 1 hour at room temperature. The embryos were then washed in Triton wash buffer and transferred to a drop of ice-cold calcium isolation buffer (2 mM CaCl2 in wash buffer) and incubated at 4 °C for 30 minutes or 2 hours for targeted chromatin digestion. An equal volume of 2× EGTA-STOP buffer (340 mM NaCl, 20 mM EDTA pH 8.0, 10 mM EGTA pH 8.0, 50 μg/mL glycogen, 50 μg/mL RNaseA, 0.05% Triton-X) was added to stop the reaction. The embryos were then incubated at 37 °C for 30 minutes to release digested chromatin fragments, and the supernatant was carefully collected. DNA extraction was performed using the QIAquick kit, and the purified CUT&RUN DNA was stored at -20 °C. Illumina library preparation was performed as previously described[87] with 15 or 18 PCR cycles. Libraries were then sequenced in 150 bp paired-end mode on the NovaSeq6000 platform.

CUT&Tag library generation and sequencing

CUT&Tag (Cleavage Under Targets & Tagmentation) for H3K4me3 was performed as previously described,[88] with modifications for embryos. Briefly, 60 to 80 late 2-cell embryos with intact zona pellucida were collected 48h post-hCG, permeabilized with a Triton-X-containing buffer, and incubated overnight at 4 °C with primary antibody (anti-H3K4me3: EpiCypher, 13-0041; 1:100 dilution). This was followed by a 30-minute incubation at room temperature with a secondary antibody (Guinea Pig anti-rabbit IgG, AntibodiesOnline, ABIN101961). After incubation with the pA-Tn5 adaptor complex (Diagenode, C01070001) for 1 hour at room temperature, tagmentation was carried out for 1 hour at 37 °C in a MgCl2-containing buffer. DNA was then extracted by incubating with a 0.1% SDS-containing buffer for 1 hour at 58 °C. SDS was neutralized with Triton-X, and the PCR reaction was conducted directly. After 18 cycles of PCR amplification using NEBNext High-Fidelity 2X PCR Master Mix (M0541), the PCR product was cleaned and size-selected using AMPure XP (Beckman Coulter). Samples were sequenced using the Illumina NovaSeq6000 platform in 150 bp paired-end mode.

Analysis of CUT&RUN and CUT&Tag data

Paired-end reads were trimmed by cutadapt[78] (version 3.4) with parameters -a CTGTCTCTTATA -A CTGTCTCTTATA -a AGATCG GAAGAGC -A AGATCGGAAGAGC—minimum-length=20. After trimming, reads were aligned to the mouse reference (GRCm38) using bowtie2 (version 2.3.5) with parameters –end-to-end –very-sensitive –no-unal –no-mixed –no-discordant -I 10 -X 500. Reads were filtered by mapping quality score using samtools (version 1.3) with parameter -q 12. Read pairs were read into R (version 4.1.2) using the readGAlignmentPairs function from the GenomicAlignment package (version 1.30) and were filtered for unique fragments. Fragments aligned to the mitochondrial genome or small scaffolds were not considered in the analysis. Fragments were counted in 100-kb consecutive genomic bins (same bin size as for DamID profiles), normalized by the sum of the fragment counts, and multiplied by a million. For chromosomal tracks, replicates were averaged, and normalized counts were visualized along the genomic coordinates. To call broad H3K9me3 domains, a two-state hidden Markov model (HMM)[76] was applied to the normalized counts. For other subsequent analyses, normalized counts were log_2 transformed after adding a pseudo-count of 0.1.

Analysis of public chromatin datasets

Published datasets were downloaded from GEO with accession numbers GSE66581[51] (ATAC-seq), GSE71434[52] (H3K4me3 ChIP), GSE112834[53] (H3K36me3 ChIP), GSE72784[54] (H3K27ac ChIP), GSE98149[33] (H3K9me3 ChIP), GSE76687[37] (H3K27me3 ChIP) and GSE135457[55] (Pol2 Stacc-seq), GSE76642[56] (DNaseI-seq). Chromatin datasets were processed and analyzed as the CUT&RUN and CUT&Tag data. For heatmap visualizations, log_2 normalized counts were scaled (centered to the genome-wide mean and divided by the standard deviation), and the median of genomic bins with significantly increased or decreased DamID OE values was taken.

Hi-C data analysis

Hi-C compartment coordinates and scores were obtained from GEO with accession GSE82185[57] and analyzed as previously described.[24]

Immunofluorescence

Embryos were fixed in 4% PFA for 20 min at room temperature and permeabilized in PBS containing 0.5% Triton-X for 20 min. Embryos were kept in blocking buffer (3% BSA in PBS) for 4-5 h and then incubated overnight in primary antibody (H3K27me3, Millipore, 07-449, 1:250; H4K20me3: Millipore, 07-463, 1:250; H3K9me2: Abcam, ab1220, 1:250 or Active Motif, 39239, 1:250; H3K9me3: Abcam, ab8898, 1:250 or Active Motif 39286, 1:100; H3K9ac: Abcam, ab4441, 1:250; H3K4me3: Abcam, ab8580, 1:250 or Diagenode, C15410003, 1:250; H3K27me2: Abcam, ab24684, 1:250; HA-tag: Roche, 11867423001, 1:500) diluted in blocking buffer. After overnight incubation, samples were washed three times in PBS and stained with secondary antibodies conjugated with (Alexa Fluor 594, Alexa Fluor 555 or Alexa Fluor 647) in blocking buffer for 2-3 h. After washing three times in PBS, embryos were mounted in Vectashield containing DAPI (Vector Laboratories). Confocal imaging was performed using a 40× oil objective in a Leica SP8 confocal microscope.

DNA FISH

DNA FISH was performed as previously described.[24,89] In brief, BACs (Table S1) were obtained from BACPAC (https://bacpacresources.org/home.htm), purified with NucleoBond BAC 100 kit (Macherey-Nagel) and nick-translated with dUTPs conjugated to ATTO550, ATTO594 or ATTO647N (Jena Bioscience). To combine nuclear lamina staining with DNA FISH, we performed immunostaining with an anti-LaminB1 antibody (Santa Cruz, sc-6216, 1:100) as described above, followed by postfixation in 2% PFA for 10 min at 37 °C. Next, embryos were briefly permeabilized (0.5% Triton-X 100, 0.02% RNaseA and 1 mg/mL PVP in PBS) for 10 min at room temperature and treated with HCl solution (0.1N HCl, 0.7% Triton-X 100 and 1 mg/mL PVP in water) for 1 min and equilibrated into prehybridization buffer (10% dextran sulphate, 2× SSC, 0.5 mM EDTA, 50% formamide, 1 mg/mL PVP, 0.05% Triton-X, 0.5 mg/mL BSA) at 55 °C for one hour. Embryos were incubated in hybridization buffer containing 1 μg/μL mouse Cot-1 DNA, denatured at 83 °C for 10 min and blocked at 37 °C for one hour. Lastly, embryos were transferred into drops of hybridization buffer containing a mixture of probes, each at 250 ng/μL which were previously denatured at 83 °C for 10 min under mineral oil. After overnight hybridization at 37 °C on a dry-bath, embryos were washed once in 2× SSC, 0.1% Triton-X 100, 1 mg/mL PVP at room temperature followed by washing three times for 10 min in 0.2× SSC, 0.01% Triton-X 100, 1 mg/mL PVP at 52 °C and mounted in Vectashield containing DAPI (Vector Laboratories) on a high precision (170 μm +/- 5 μm) glass bottom dish (Ibidi) to preserve 3D structure.

DNA FISH image analysis

Microscopy images were acquired on a Leica SP8 point scanning confocal equipped with a Plan Apochromat 100×/1.4 NA oil objective at a voxel size of 0.025 × 0.025 × 0.3 μm (x, y, z). For distance analysis, DNA FISH foci and LaminB1 signals were segmented from unadjusted raw images using Ilastik[81] and analyzed using a custom Python script. The script segments nuclear boundaries (LaminB1 signal), identifies and filters FISH signals, and calculates distances between FISH signal centroids, the nuclear surface and the center of the nucleus (defined as the inner volume encapsulated by LaminB1). These distance measurements were then used to compute the distance ratio (dRatio) by taking the shortest distance from the DNA FISH centroid to LaminB1 and dividing it by the total distance. The total distance is the sum of two parts: the distance from the center of the nucleus to the DNA FISH signal,

Cell
Resource

CellPress
OPEN ACCESS

and the shortest distance between the DNA FISH signal and LaminB1. a *dRatio* close to 1 indicates proximity to the center of the nucleus, while a *dRatio* close to 0 indicates proximity to the nuclear periphery. *dRatio* was compared to the $\log_2$ mean DamID OE values of the overlapping genomic bins. Representative images are shown as a maximum intensity projection of two to three z-stacks (0.3 μm), in which noise was smoothed with a Gaussian blur on LaminB1 and the FISH signal (sigma 1.0 and 2.0 radius, respectively) uniformly across all images equally and contrast/brightness adjusted and thus fluorescence intensity is not comparable across the images presented in the Figures.

QUANTIFICATION AND STATISTICAL ANALYSIS

All statistical analysis was performed using R (versions are indicated for each analysis). To identify differential DamID signals between treatment and control conditions, a generalized linear model of the gamma family with log link was fitted on the replicate OE values for each genomic bin in R (version 4.1.2). P-values were calculated based on the z-distribution and were adjusted for multiple comparisons by the Benjamini & Hochberg method. Significant bins were called by an adjusted p-value cutoff of 0.01 and a $\log_2$ fold change cutoff of 1. For analysis of RNA-seq data, differentially expressed genes were called with a cutoff of 0.05 on adjusted p-values from DESeq2 (version 1.26.0). Smoothing of metaplot profiles in Figures 1E, 3D, 4E, 4F, 5D, 5H, 6C–6F, 6I–6L, 6N, 7B, 7C, S6G, S6H, and S7D was done by fitting a local polynomial regression model with span=0.4 (except for Figures 4F and 6I–6K, span=0.2) on the average OE values using the loess function in R (version 4.1.2). Boxplots in Figures 1F, 2E, 3E, S1F, S1H–S1J, S3E, S5D, S5G, S6D, and S6E show the median, and the interquartile range (IQR), and whiskers depict the smallest and largest values within 1.5×IQR. In Figures 2E, S6D, and S6E, the number of 100-kb genomic bins analyzed is indicated. In Figure S1H, n indicates number of pronuclei analyzed for size quantification. In Figures S1D, S3D, S5B, and S5E, inside violin plots, the 25th and 75th percentiles (black lines) and the median (dot) are shown. Below the violin plots, n indicates number of LADs. Hierarchical clustering was performed by pheatmap (version 1.0.12) in R using Manhattan distance with ward.D method in Figures 2A, 4A, 5B, and 5F, Euclidean distance with ward.D method in Figures 2C, 4C, S2A, S2B, S4A, S4B, and S4D, and Euclidean distance with complete method in Figures 2D, 4D, 6A, 6B, S2C, S4C, S6B, and S6C. For immunostainings, all conditions for a particular experiment were processed and acquired together and images were processed using the same settings for representation with Fiji.[80] For all embryo experiments, N indicates number of independent biological replicates. In immunostainings and developmental assay experiments, n indicates the number of embryos analyzed. For DNA FISH experiments, n indicates number of FISH spots analyzed. For quantification of pronuclear (PN) size in Figure S1H, the PN size was determined by the DAPI area on maximum-intensity projection images using Fiji. Relative pronuclear size was calculated by normalizing the size of each pronucleus over the mean size of control paternal pronucleus, which was set to 1. Pairwise Wilcoxon rank-sum test was performed, where indicated p is adjusted p-value for multiple comparisons. Additional statistical details for experiments can be found in the corresponding figure legends.
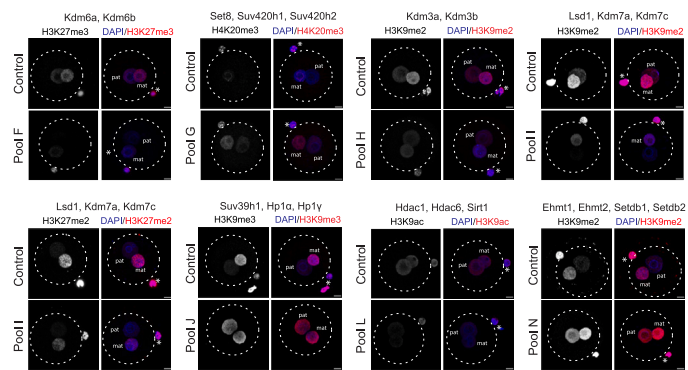
Supplemental figures

(legend on next page)
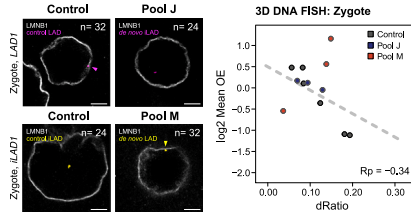
Figure S1. Detail of phase I screening, validation, and allelic analysis of DamID dataset in zygotes, related to Figure 1

(A) Brief description of the candidates investigated in this study and pooling of those for phase I of screening. Information about the dominant-negative (DN) constructs is shown below with references.

(B) Representative maximum intensity projections of confocal images from immunostainings of the indicated histone modifications in late zygotes (28–30 h post-hCG injection) from control or experimental groups. Dashed lines roughly demarcate the plasma membrane. DNA was counterstained with DAPI. On the merged images, asterisks indicate the polar body. Scale bars, 10 μm. $N \geq 2$; $n \geq 10$. Mat, maternal pronucleus; pat, paternal pronucleus.

(C) (Left) Representative confocal images of immuno-3D FISH in late zygotes for LaminB1 (LMNB1) and genomic regions within LADs or iLADs as indicated. Regions corresponding to LADs and iLADs in control embryos are shown in purple and yellow, respectively. Arrowheads point to DNA-FISH spots localizing at nuclear lamina. Scale bars, 5 μm. n = number of DNA-FISH spots analyzed. Data derive from two biologically independent experiments. (Right) Correlation between DamID values and distance measurements from DNA FISH of all indicated datasets (control, pools J and M). The y axis is the $\log_2$ transformed mean OE values for genomic loci corresponding to selected LADs and iLADs derived from the DamID replicates. The x axis indicates the average distance ratio (dRatio) of the individual FISH probes determined from at least 24 measurements ($24 \leq n \leq 44$). A dRatio close to 1 indicates proximity to the center of the nucleus, while a dRatio close to 0 indicates proximity to the nuclear periphery. Pearson's correlation (Rp) is indicated. Note the overall negative correlation between DamID values and distance to the nuclear periphery, as expected.

(D) Distribution of zygotic LAD length. Violin plots show the 25th and 75th percentiles (black lines) and median (circles). n indicates the number of LADs called, shown below violin plots. The candidate pools are arranged in a descending order based on median LAD size, and control is highlighted in yellow.

(E) Percentage genomic coverage of LADs and iLADs. The candidate pools are arranged in a descending order of LAD coverage, and control is highlighted in yellow.

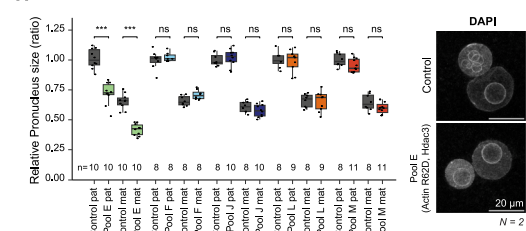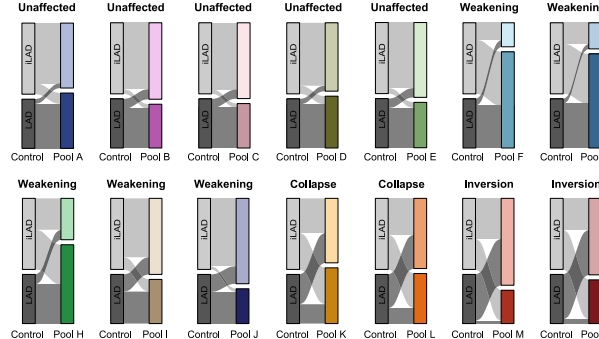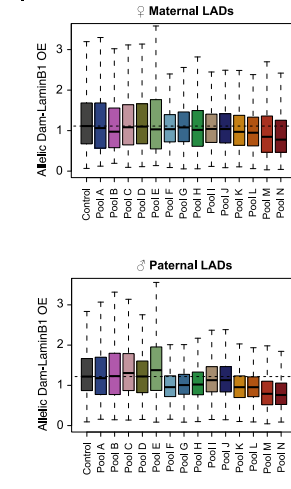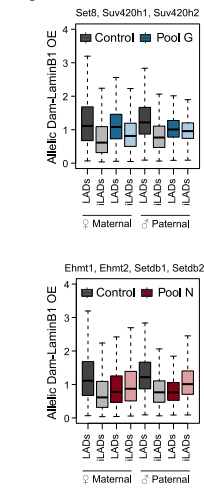(F) Boxplots of Dam-LaminB1 OE mean values in control and de novo called LAD and iLAD regions. The horizontal dotted lines indicate the median OE values from the control zygotic LADs (upper line) and iLADs (lower line).

(G) Alluvial plot showing zygotic LAD reorganization upon perturbations performed with respect to the control.

(H) Quantification of pronuclear area across several pools in phase I screening. n = number of pronuclei analyzed from two independent experiments (N = 2). Pairwise Wilcoxon rank-sum test was performed, and *** indicates $p < 0.001$, where p is adjusted p value for multiple comparisons. Representative maximum intensity projections of DAPI staining in late zygotes are shown for pool E and control. Scale bars, 20 μm; ns, non-significant ($p > 0.05$). mat, maternal pronucleus; pat, paternal pronucleus.

(I and J) Boxplots of allelic (paternal and maternal) Dam-LaminB1 OE mean values from hybrid zygotes (C57BL/6J × CBA/H female × DBA/2J male) in control LAD and iLAD regions. Only genomic bins containing more than 30 allelic GATC reads were analyzed. The number of 100-kb genomic bins analyzed are n = 1,835 for maternal LADs, 2,419 for maternal iLADs, 1,446 for paternal LADs, and 2,808 for paternal iLADs. The horizontal dotted lines in (I) indicate the median allelic OE values from the control maternal or paternal LADs. The allelic LAD and iLAD coordinates used for this analysis were extracted from GEO: GSE112551.

A

Overlap of regions with increased DamID scores in zygote

Pool M (H1.2, H1.4, H1.5, macroH2A)
Pool N (Ehmt1, Ehmt2, Setdb1, Setdb2)
Pool K (Phf19, G2e3, Dhx33)
Pool L (Hdac1, Hdac6, Sirt1)
Pool G (Set8, Suv420h1, Suv420h2)
Pool I (Lsd1, Kdm7a, Kdm7c)
Pool F (Kdm6a, Kdm6b)
Pool H (Kdm3a, Kdm3b)
Pool J (Suv39h1, Hp1α, Hp1γ)
Pool C (Tpr, DN Nup98)
Pool E (Actin R62D, Hdac3)
Pool A (DN Baf, DN Prr14, DN Syne1)
Pool B (Exportin6, cVCA Actin)
Pool D (DN NM1, DN MyosinVb)

number of genomic bin overlaps
0   500   1000   1500

B

Overlap of regions with decreased DamID scores in zygote

Pool E (Actin R62D, Hdac3)
Pool D (DN NM1, DN MyosinVb)
Pool B (Exportin6, cVCA Actin)
Pool C (Tpr, DN Nup98)
Pool A (DN Baf, DN Prr14, DN Syne1)
Pool I (Lsd1, Kdm7a, Kdm7c)
Pool J (Suv39h1, Hp1α, Hp1γ)
Pool F (Kdm6a, Kdm6b)
Pool G (Set8, Suv420h1, Suv420h2)
Pool H (Kdm3a, Kdm3b)
Pool M (H1.2, H1.4, H1.5, macroH2A)
Pool N (Ehmt1, Ehmt2, Setdb1, Setdb2)
Pool K (Phf19, G2e3, Dhx33)
Pool L (Hdac1, Hdac6, Sirt1)

number of genomic bin overlaps
0   100   200   300   400   500

C

Chromatin features of regions with decreased DamID scores in zygote

Pool C (Tpr, DN Nup98)
Pool B (Exportin6, cVCA Actin)
Pool E (Actin R62D, Hdac3)
Pool A (DN Baf, DN Prr14, DN Syne1)
Pool D (DN NM1, DN MyosinVb)
Pool I (Lsd1, Kdm7a, Kdm7c)
Pool J (Suv39h1, Hp1α, Hp1γ)
Pool N (Ehmt1, Ehmt2, Setdb1, Setdb2)
Pool G (Set8, Suv420h1, Suv420h2)
Pool F (Kdm6a, Kdm6b)
Pool L (Hdac1, Hdac6, Sirt1)
Pool M (H1.2, H1.4, H1.5, macroH2A)
Pool H (Kdm3a, Kdm3b)
Pool K (Phf19, G2e3, Dhx33)

LADs Control zygote
iLADs Control zygote

H3K9me3 oocyte
H3K9me3 zygote
H3K27me3 oocyte
H3K27me3 zygote
H3K4me3 oocyte
H3K4me3 zygote
H3K36me3 oocyte
H3K36me3 zygote
H3K27ac oocyte
DNase-seq zygote
ATAC-seq early 2-cell
Pol2 zygote
Compart. zygote

median enrichment
-1   -0.5   0   0.5   1

Figure S2. Overlap of genomic regions affected in phase I screening with pooled candidates in zygotes and associated chromatin features, related to Figure 2

(A) Heatmap showing overlap of genomic regions that show increased Dam-LaminB1 OE values (up) in zygote with respect to control.

(B) Heatmap showing overlap of genomic regions that show significantly reduced Dam-LaminB1 OE values (down) in zygote with respect to control.

(C) Heatmap showing enrichment of chromatin features in genomic regions that lose lamina interactions (down) compared with controls in zygote. Chromatin feature enrichment in LADs and inter-LADs (iLADs) of control zygotes is shown below for comparison. Positive compartment scores (Compart.) define A-compartment.

A

Kdm6a, Kdm6b
H3K27me3 DAPI/H3K27me3

Set8, Suv420h1, Suv420h2
H4K20me3 DAPI/H4K20me3

Kdm3a, Kdm3b
H3K9me2 DAPI/H3K9me2

Lsd1, Kdm7a, Kdm7c
H3K9me2 DAPI/H3K9me2

Lsd1, Kdm7a, Kdm7c
H3K27me2 DAPI/H3K27me2

Suv39h1, Hp1α, Hp1γ
H3K9me3 DAPI/H3K9me3

Hdac1, Hdac6, Sirt1
H3K9ac DAPI/H3K9ac

Ehmt1, Ehmt2, Setdb1, Setdb2
H3K9me2 DAPI/H3K9me2

B

3D DNA FISH: 2-cell

C

D

E

Pool A 2-cell
DN Baf, DN Prr14, DN Syne1

Pool C 2-cell
Tpr, DN Nup98

Pool D 2-cell
DN NM1, DN MyosinVb

Pool F 2-cell
Kdm6a, Kdm6b

Pool G 2-cell
Set8, Suv420h1, Suv420h2

Pool H 2-cell
Kdm3a, Kdm3b

Pool K 2-cell
Phf19, G2e3, Dhx33

Pool M 2-cell
H1.2, H1.4, H1.5, macroH2A

F
Single Plane; HA-tag: H1.2/4/5, macroH2A

G

H
Combined PCA of zygote and 2-cell

I

DN Baf, DN Prr14, DN Syne1

Tpr, DN Nup98

DN NM1, DN MyosinVb

Actin R62D, Hdac3

Kdm6a, Kdm6b

Set8, Suv420h1, Suv420h2

Kdm3a, Kdm3b

Phf19, G2e3, Dhx33

Hdac1, Hdac6, Sirt1

Lsd1, Kdm7a, Kdm7c

Suv39h1, Hp1α, Hp1γ

LAD reorganization phenotype groupings

H1.2, H1.4, H1.5, macroH2A

Ehmt1, Ehmt2, Setdb1, Setdb2

(legend on next page)

Figure S3. Analysis of phase I screening and validation in 2-cell-stage embryos, related to Figure 3

(A) Representative confocal images showing maximum intensity projections from immunostainings of the indicated histone modifications in control and experimental late 2-cell-stage embryos (48–50 h post-hCG injection). Dashed lines roughly demarcate the contour of the embryos. DNA was counterstained with DAPI. On the merged images, asterisks indicate the polar body. Scale bars, 10 μm. $N \geq 2$; $n \geq 10$.

(B) (Left) Representative confocal images of immuno-3D FISH in late 2-cell-stage embryos for LaminB1 (LMNB1) and genomic regions within LADs or iLADs as indicated. Regions corresponding to iLADs in control embryos are shown in yellow. Arrowheads point to DNA-FISH spots localizing at nuclear lamina. Scale bars, 5 μm. n = number of DNA-FISH spots analyzed. Data derive from two biologically independent experiments. (Right) Correlation between DamID values and distance measurements from DNA FISH of all indicated datasets (control, pools J and M). The y axis is the log$_2$ transformed mean OE values for genomic loci corresponding to selected LADs and iLADs derived from the DamID replicates. The x axis indicates the average distance ratio (*dRatio*) of the individual FISH probes determined from at least 17 measurements ($17 \leq n \leq 33$). A *dRatio* close to 1 indicates proximity to the center of the nucleus, while a *dRatio* close to 0 indicates proximity to the nuclear periphery. Pearson's correlation (Rp) is indicated. Note the overall negative correlation between DamID values and distance to the nuclear periphery, as expected.

(C) Distribution of LAD length in 2-cell embryos. Violin plots show the 25th and 75th percentiles (black lines) and median (circles). n indicates the number of LADs called, shown below violin plots. The candidate pools are arranged in a descending order based on median LAD size, and control is highlighted in yellow.

(D) Percentage genomic coverage of LADs and iLADs. The candidate pools are arranged in a descending order of LAD coverage in 2-cell embryos, and control is highlighted in yellow.

(E) Boxplots of Dam-LaminB1 OE mean values in control and *de novo* called LAD and iLAD regions. The horizontal dotted lines indicate the median OE values from the control 2-cell LADs (upper line) and iLADs (lower line).

(F) Representative single confocal images from immunostaining using an HA-antibody in late 2-cell-stage embryos. In pool M, all histones (H1.2, H1.4, H1.5, and macroH2A) contain an N-terminal HA tag. Scale bars, 10 μm. $N \geq 2$; $n \geq 10$.

(G) Representative confocal images from maximum intensity projections from H3K9me2 immunostainings in late 2-cell-stage embryos in control or embryos from pools M and N. Scale bars, 10 μm. $N \geq 2$; $n \geq 10$.

(H) Combined PCA of all zygotic and 2-cell DamID samples from phase I screening. Each data point represents the mean of the biological replicates for the corresponding manipulation indicated by the color code. The percentage of variance explained by PC1 and PC2 is indicated in axis labels.

(I) Alluvial plots showing the reorganization of genomic regions between LAD and iLAD during the MZT and how that is affected upon perturbations with respect to the control zygote and 2-cell embryos. LAD reorganization phenotype groupings (U-U/W, W-U/W, W-C, C-U/W, and I-C) are explained below the plots.

A Overlap of regions with increased DamID scores in 2-cell

B Overlap of regions with decreased DamID scores in 2-cell

C Chromatin features of regions with decreased DamID scores in 2-cell

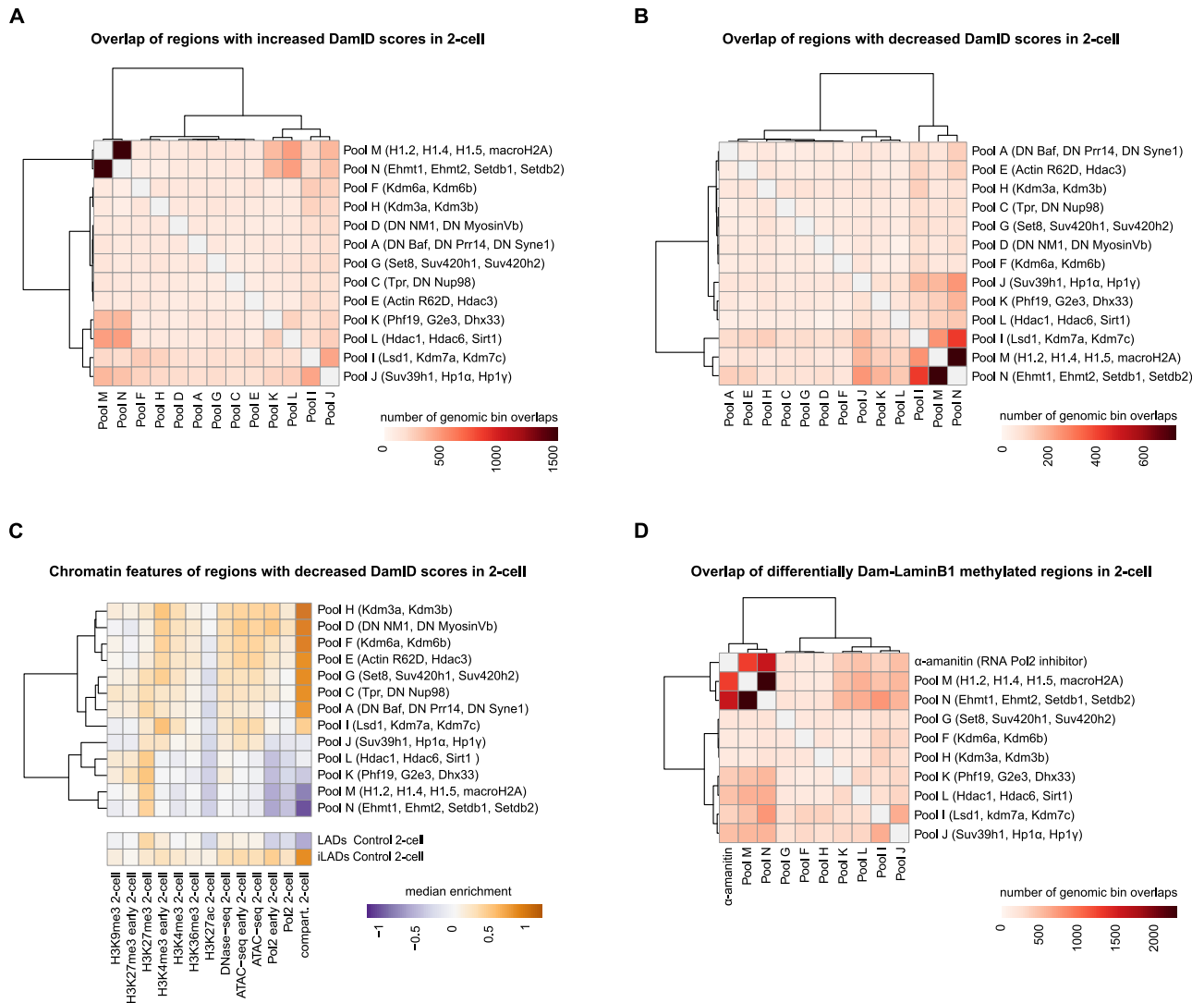**D** Overlap of differentially Dam-LaminB1 methylated regions in 2-cell

Figure S4. Overlap of genomic regions affected in phase I screening with pooled candidates in 2-cell-stage embryos and associated chromatin features, related to Figure 4

(A) Heatmap showing overlap of genomic regions that show significantly increased Dam-LaminB1 OE values (up) in phase I screening samples with respect to control at the 2-cell stage.

(B) Heatmap showing overlap of genomic regions that show significantly reduced Dam-LaminB1 OE values (down) with respect to control in 2-cell embryo samples.

(C) Enrichment of chromatin features in genomic regions that lose lamina interactions (down) compared with controls in 2-cell-stage embryos. Chromatin feature enrichment in control 2-cell LADs and inter-LADs (iLADs) is shown below for comparison. Positive compartment scores (Compart.) define A-compartment.

(D) Heatmap showing overlap of all genomic bins that show differential lamina interactions (up + down) in 2-cell-stage embryos with respect to controls comparing α-amanitin treatment to DamID samples from screening phase I where different chromatin pathways are targeted with pooled candidates.

A

B LAD size: Zygote

C LAD coverage: Zygote

D

E LAD size: 2-cell

F LAD coverage: 2-cell

G

H
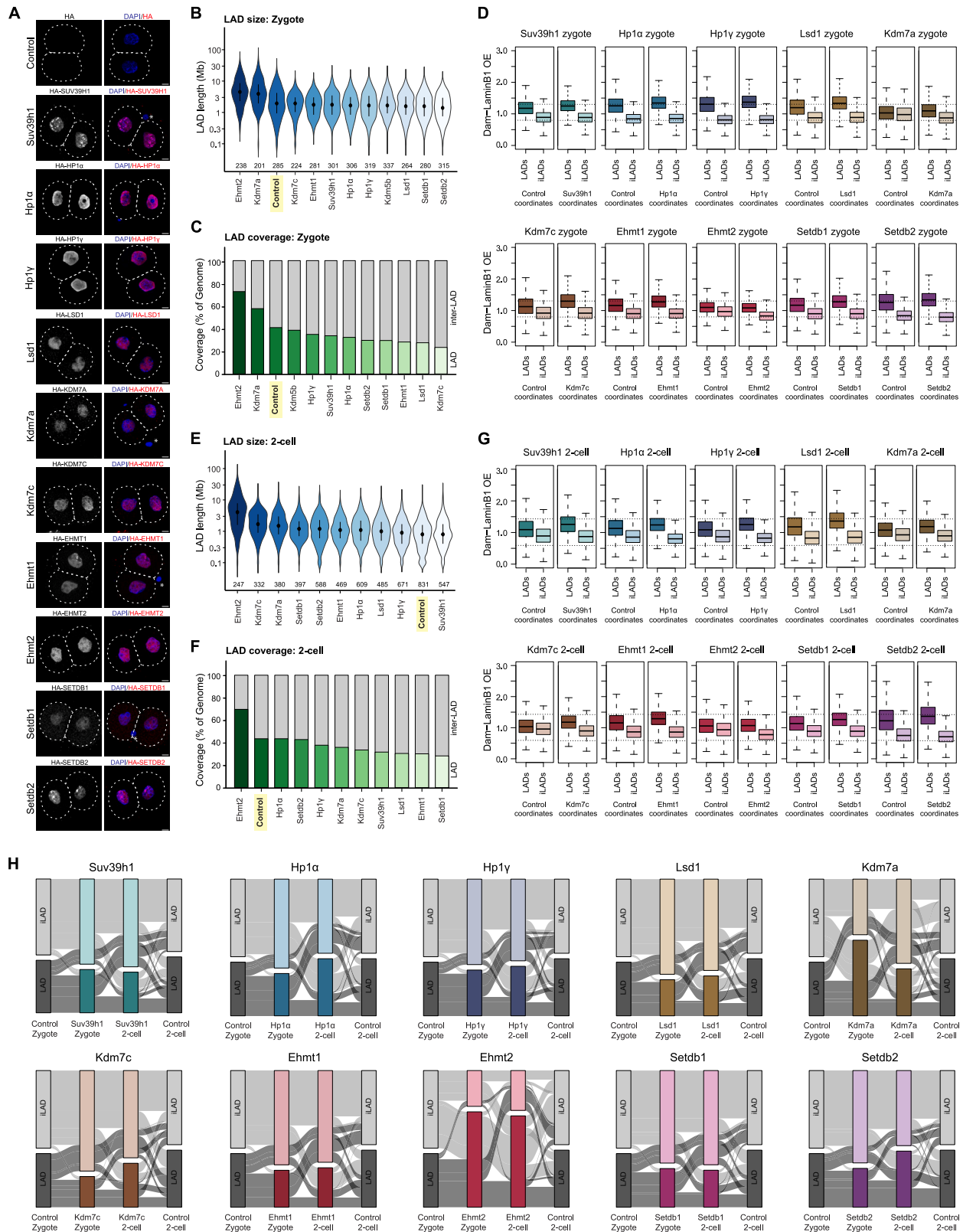
(legend on next page)

Figure S5. Analysis of phase II screening with individual hits and validation in zygotes and 2-cell-stage embryos, related to Figure 5

(A) Representative confocal images showing maximum intensity projections from immunostaining using an HA-antibody in late 2-cell-stage embryos (48–50 h post-hCG injection). All candidates expressed in the phase II screening contain N-terminal HA tag. Dashed lines roughly demarcate the cell membrane. DNA was counterstained with DAPI. On the merged images, asterisks indicate the polar body. Scale bars, 10 μm. $N \geq 2$; $n \geq 10$.

(B) Distribution of zygotic LAD length in phase II screening samples. Violin plots show the 25th and 75th percentiles (black lines) and median (circles). n indicates the number of LADs called, shown below violin plots. The candidates are arranged in a descending order based on median LAD size, and control is highlighted in yellow.

(C) Percentage genomic coverage of LADs and iLADs in zygotes. The candidates are arranged in a descending order of LAD coverage, and control is highlighted in yellow.

(D) Boxplots of Dam-LaminB1 OE mean values in control and *de novo* called LAD and iLAD regions for zygotes. Box plots show the median and the interquartile range (IQR), and whiskers depict the smallest and largest values within 1.5 × IQR. The horizontal dotted lines indicate the median OE values from the control zygotic LADs (upper line) and iLADs (lower line).

(E) Distribution of LAD length in 2-cell embryos. The candidates are arranged in a descending order based on median LAD size, and control is highlighted in yellow.

(F) Percentage genomic coverage of LADs and iLADs in 2-cell embryos. The candidates are arranged in a descending order of LAD coverage, and control is highlighted in yellow.

(G) Boxplots of Dam-LaminB1 OE mean values in control and *de novo* called LAD and iLAD regions for 2-cell embryos. The horizontal dotted lines indicate the median OE values from the control 2-cell LADs (upper line) and iLADs (lower line).

(H) Alluvial plots showing the reorganization of genomic regions between LAD and iLAD during the MZT and how that is affected upon candidate expression with respect to the control zygote and 2-cell embryos.

A

Suv39h1 zygote | Hp1α zygote | Hp1γ zygote | Lsd1 zygote | Kdm7a zygote | Suv39h1 2-cell | Hp1α 2-cell | Hp1γ 2-cell | Lsd1 2-cell | Kdm7a 2-cell

Kdm7c zygote | Ehmt1 zygote | Ehmt2 zygote | Setdb1 zygote | Setdb2 zygote | Kdm7c 2-cell | Ehmt1 2-cell | Ehmt2 2-cell | Setdb1 2-cell | Setdb2 2-cell

B Chromatin features of regions with decreased DamID scores in zygote

C Chromatin features of regions with decreased DamID scores in 2-cell

D Pool J zygote | Suv39h1 zygote | Hp1α zygote | Hp1γ zygote

E Pool J 2-cell | Suv39h1 2-cell | Hp1α 2-cell | Hp1γ 2-cell

F

G DamID Zygote

H DamID 2-cell

I

J PCA: H3K9me3 CUT&RUN, 2-cell

K PCA: H3K4me3 CUT&Tag, 2-cell

L

M Control | Pool J | Pool I
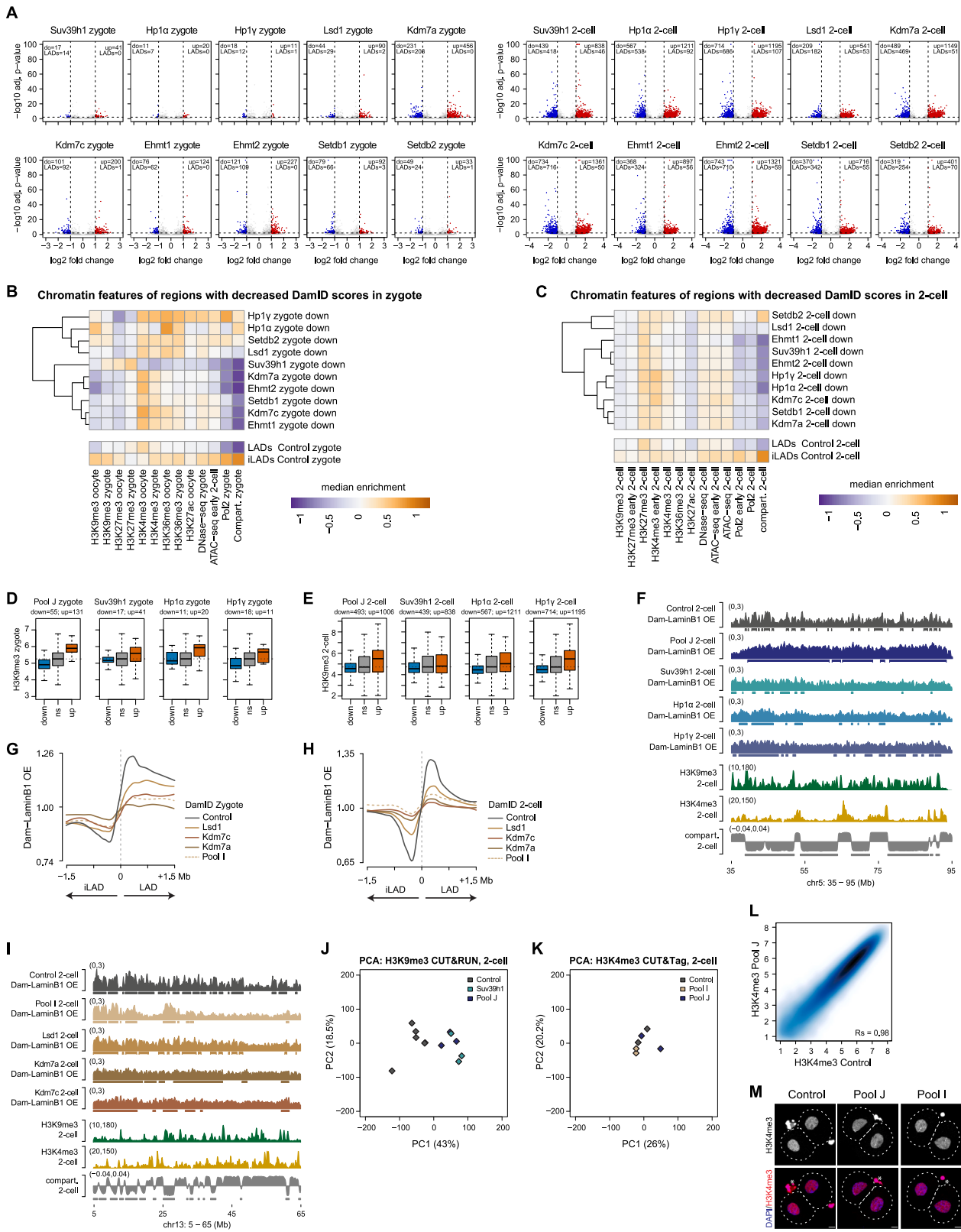
(legend on next page)

Figure S6. Differential analysis of genomic regions affected in zygotes and 2-cell embryos in phase II with individual hits, their chromatin features, and chromatin profiling, related to Figure 6

(A) Volcano plots of genomic regions that show differential Dam-LaminB1 OE values in comparison to control embryos for corresponding developmental stages (left, zygote; right, 2-cell-stage embryo). Up indicates the number of 100-kb genomic bins that have significantly higher OE values (log_2 fold change > 1 and adjusted p value < 0.01; red dots), and do (down) shows the number of genomic bins that show significantly reduced OE value (log_2 fold change < −1 and adj. p value < 0.01; blue dots). The number of up or do genomic bins that belong to LADs in control embryos is indicated below.

(B) Heatmap showing enrichment of chromatin features in genomic regions that lose lamina interactions (down in volcano plots) compared with controls in zygotic DamID samples when candidate effectors are expressed. Chromatin feature enrichment in zygotic LADs and inter-LADs (iLADs) in control embryos is shown below for comparison. Positive compartment scores (Compart.) define A-compartment.

(C) Enrichment of chromatin features in genomic regions that lose lamina interactions (down in volcano plots) compared with controls in 2-cell-stage samples.

(D and E) Box plots showing log_2 transformed H3K9me3 enrichment in genomic regions that gain (up) or lose (down) OE value compared with controls in zygote (E) and 2-cell-stage (F) embryos. Box plots show the median and the interquartile range (IQR), and whiskers depict the smallest and largest values within 1.5 × IQR. Number of 100-kb genomic bins analyzed is indicated. ns, genomic regions with non-significant changes in lamina association. The horizontal dotted lines indicate the median signal in the ns genomic regions for the corresponding analysis. The H3K9me3 data are publicly available and derive from control zygote and 2-cell-stage embryos.

(F and I) Dam-LaminB1 OE value, histone modification enrichment, and compartment score from 2-cell-stage embryos calculated from publicly available datasets. Boxes under the OE value tracks represent called LADs, and wild-type 2-cell B-compartment regions are indicated below the compartment score tracks.

(G and H) Average Dam-LaminB1 OE value over control LAD boundaries across different DamID samples for zygote (G) and 2-cell-stage (H) embryos comparing individual effectors (Kdm7a, Kdm7c, Lsd1, solid lines) to candidate pools (pool I, dotted line).

(J) PCA on all H3K9me3 CUT&RUN samples and replicates from late 2-cell stage. CUT&RUN was performed in at least two independent biological replicates. Data points are colored based on the experimental conditions as indicated.

(K) PCA on H3K4me3 CUT&Tag samples. CUT&Tag was performed at the late 2-cell stage in two independent biological replicates. Data points are colored based on the experimental conditions as indicated.

(L) Smoothed scatter plot of genome-wide H3K4me3 enrichment values (log_2 transformed). Spearman's correlation (Rs) is indicated.

(M) Representative confocal images from maximum intensity projections from immunostaining against H3K4me3 in late 2-cell-stage embryos (48–50 h post-hCG injection). Dashed lines roughly demarcate the cell membrane. DNA was counterstained with DAPI. On the merged images, asterisks indicate the polar body. Scale bars, 10 μm. $N \geq 2$; $n \geq 10$.
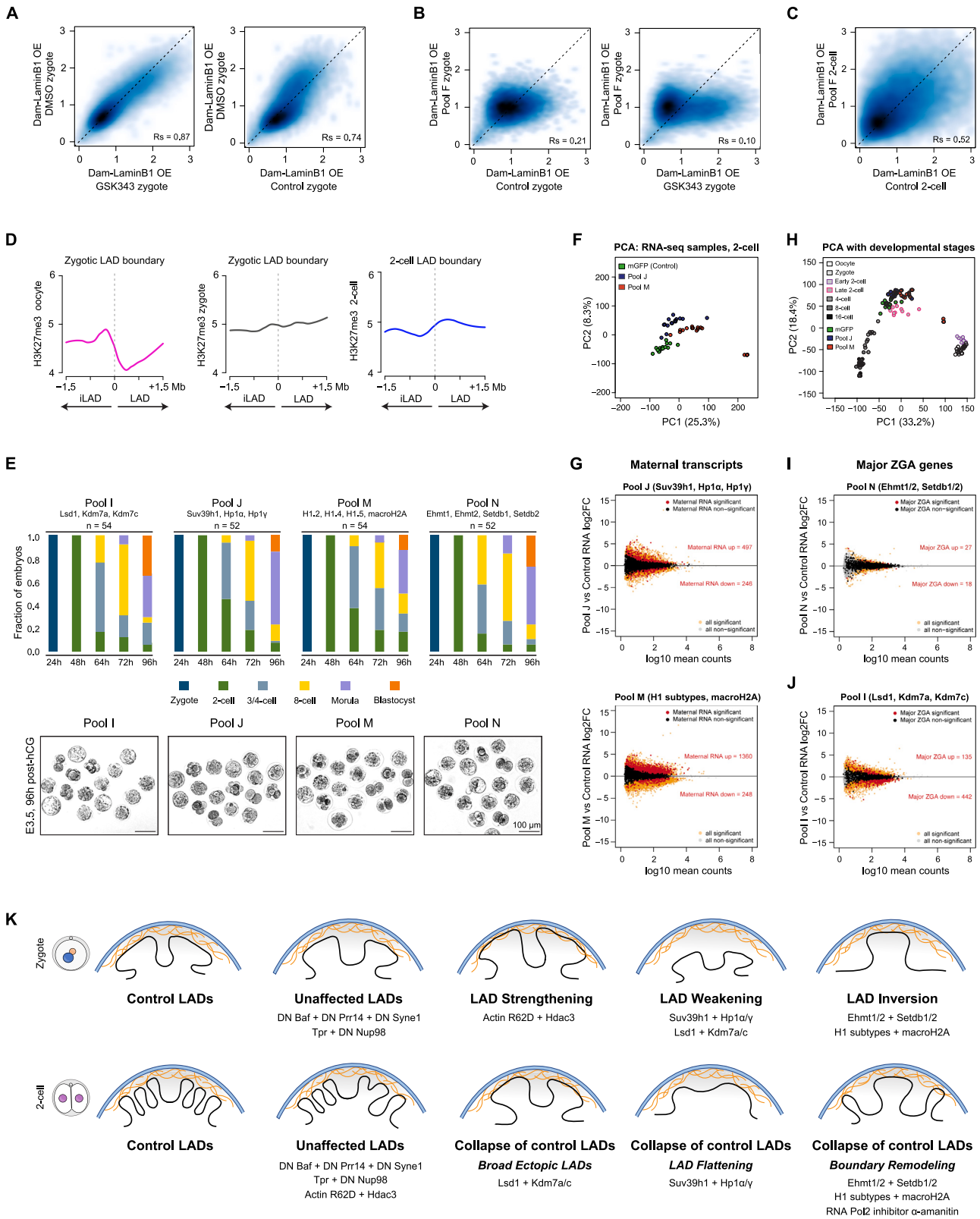
(A–C) Smoothed scatter plot of genome-wide Dam-LaminB1 OE mean values. Spearman's correlation (Rs) is indicated.

(D) Average H3K27me3 enrichment ($\log_2$ transformed) signal from publicly available datasets over LAD boundaries. Zero and the dotted line represent the position of the LAD/iLAD boundary in the metaplot. The 1.5 Mb region toward the right-hand side indicates LAD.

(E) Developmental progression (in percentage) of embryos from the indicated pools. Embryos were microinjected with mRNAs for each pool at the zygote stage, and developmental progression was monitored daily. Plotted is the fraction of embryos at the indicated stage corresponding to the time post-hCG injection in h (x axis). Representative images after 3.5 days in culture (E3.5; corresponds to 96 h post-hCG). n = number of embryos analyzed. Data derive from at least three independent experiments. Scale bars, 100 μm. Developmental data for control (mGFP-injected) embryos are shown in Figure 7F.

(F) PCA of late 2-cell-stage single-embryo RNA-seq read counts (genes and transposable elements combined) across experimental and control samples as indicated. Embryos (n = 16) were collected from two independent biological experiments. The variance explained (percentage) is indicated along the PC1 and PC2 axes.

(G) MA plots of $\log_2$-fold change in transcript abundance (RNA-seq counts) for 2-cell-stage embryos against mean RNA-seq counts ($\log_{10}$ transformed). Differentially expressed genes are labeled in orange (adj. p value < 0.05), and non-differential genes are in gray. Differentially expressed (adj. p value < 0.05) maternal transcripts (as per DBTMEE classification) are marked in red, non-differential ones are in black.

(H) Combined PCA of RNA-seq read counts for control (mGFP), pools J and M embryos in comparison with non-manipulated embryos from oocytes to 16-cell stage (GEO: GSE225056). Each dot is an embryo, and the conditions are displayed by the indicated color code.

(I and J) MA plots of $\log_2$-fold change in transcript abundance for pools N (I) and I (J) embryos in late 2-cell stage. Differentially expressed (adj. p value < 0.05) major ZGA genes (DBTMEE) are marked in red, and non-differential major ZGA genes are shown in black.

(K) Summary of LAD disruption phenotypes in zygote (top row) and 2-cell-stage embryos (bottom row). Blue lines depict the nuclear envelope and orange mesh the nuclear lamina. DN, dominant-negative construct. The relative strength of interactions with the nuclear lamina is represented by the distance between the nuclear lamina and the LADs.